NOVEL TECHNIQUES FOR REGISTRATION OF MULTIMODAL MEDICAL IMAGES

NIMA MASOUMI

A THESIS

IN

THE DEPARTMENT

OF

ELECTRICAL AND COMPUTER ENGINEERING

PRESENTED IN PARTIAL FULFILLMENT OF THE REQUIREMENTS

FOR THE DEGREE OF MASTER OF APPLIED SCIENCE

CONCORDIA UNIVERSITY

MONTRÉAL, QUÉBEC, CANADA

AUGUST 2018

CONCORDIA UNIVERSITY

School of Graduate Studies

This is to certify that the thesis prepared

By: **Nima Masoumi**

Entitled: **Novel techniques for registration of multimodal medical images**

and submitted in partial fulfillment of the requirements for the degree of

Master of Applied Science

complies with the regulations of this University and meets the accepted standards with respect to originality and quality.

Signed by the final examining commitee:

_____ Chair
Dr. Dongyu Qiu

_____ Internal Examiner
Dr. Habib Benali

_____ External Examiner
Dr. Abdessamad Ben Hamza

_____ Supervisor
Dr. Hassan Rivaz

Approved _____
Dr. W. E. Lynch, Chair
Department of Electrical and Computer Engineering

_____ 2018

_____
Dr. A. Asif, Dean
Faculty of Engineering and Computer Science

Abstract

Novel techniques for registration of multimodal medical images

Nima Masoumi

Medical image registration is a critical image processing task in many applications such as image-guided surgery (IGS) and image-guided radiotherapy. Herein, a novel automatic inter-modal affine registration technique is proposed based on the correlation ratio (CR) similarity metric firstly. The technique is demonstrated through registering intra-operative ultrasound (US) scans with magnetic resonance (MR) images of 22 patients from a publicly available database. By using landmark-based mean target registration errors (mTRE) for evaluation, the technique has achieved a result of 2.79$\pm$1.13 mm from an initial value of 5.40$\pm$4.31 mm. A nonparametric statistical analysis performed using the Wilcoxon rank sum test shows that there is a significant difference between pre- and post-registration mTREs with a p-value of 0.0058. To achieve this result, the MRI was deemed as the fix image (I_f) and the US as the moving image (I_m) and then I_m was transformed to align with I_f. Covariance matrix adaptation evolutionary strategy (CMA-ES) was utilized to find the optimal affine transformation in registration of I_m to I_f. In addition to quantitative validation using mTRE, the results were validated qualitatively by overlaying pre- and post-registration US and MRI to allow visual assessment of the alignment. The proposed fully automatic registration method significantly improved the alignment of MRI and US images and can therefore be used to aid neurosurgeons in resection of brain tumors. In addition to proposing new methods for registration of US and MRI, three different datasets of corresponding CT and US images of vertebrae were collected and presented. In the first dataset, two human patients lumbar vertebrae are presented and the US images are simulated from the CT images. The second dataset includes corresponding CT and US images of a phantom, made of post-mortem canine cervical and thoracic vertebrae. The third dataset

includes the CT and US images of a lambs lumbar vertebrae. For the two latter datasets, 15 corresponding landmarks were provided and fiducial registration of the corresponding images was performed to acquire a silver standard ground truth of the registration. This dataset will be released online to allow validation of US-CT registration techniques.

Acknowledgments

I would like to express my deepest appreciation to my knowledgeable, supportive, and genius supervisor, Dr. Hassan Rivaz. Without the support of him, I would not have been possible to mature my academic knowledge during my masters at Concordia University. In the harsh time of my research, he guided me to get mature and face the reality of the academic life. He provided every required equipment to proceed my research as efficient as possible.

I would also like to extend my gratitude to my colleagues in the IMPACT lab for their guides and sharing of their experiences with me. I would like to thank especially to Dr. Yiming Xiao at Robarts Research Institute for invaluable discussions to my research papers. I would like to thank also Dr. Stephen Frey and Dr. Roch Comeau from Rogue Research Inc. (Montreal, Canada) for lending us tracking equipment for collection of 3D ultrasound volumes. Thanks should also go to Elekta Ltd. (Montreal, Canada), and especially Ms. Elodie Lugez and Ms. Chantal Dussault for donating us the Northern Digital Inc. (NDI) Polaris tracking systems (Waterloo, Canada).

Special thanks to funding resources (Natural Science Engineering Council of Canada (NSERC) grant RGPIN-2015-04136) which facilitated and encouraged me to continue strongly in rise and falls of my research life. Many thanks to Dr. Habib Benali, Dr. Abdessamad Ben Hamza, and Dr. Dongyu Qiu for agreeing to serve as the thesis evaluation committee.

I am deeply indebted to my parents for their emotional support. I wish they will be always proud of me and I could pay back their deeds with my success.

Contents

List of Figures

List of Tables

Chapter 1

Introduction

In this chapter, a brief explanation about ultrasound imaging is provided first, followed by an introduction to medical image registration. Next, the objectives and contributions of this thesis are provided, and the chapter is concluded with an outline of the thesis.

1.1 Ultrasound Imaging

Similar to electromagnetic waves, sound wave can propagate with different frequencies. Normally, a human being cannot hear sound waves with frequencies higher than 20KHz. Ultrasound (US) is the sound wave with the frequencies higher than 20KHz up to several megahertz. In practice, US can be generated with ultrasonic devices and sonography or US machines. US machines are applicable in medicine for clinical and research purposes. US machines with various purposes and different characteristics are manufactured by several recognized companies, for instance General Electric (GE), Siemens, Philips. Each US machine consists of different modules including transducer, processor, and user-interfaces such as keyboard, monitor, and control buttons (Fig. 1).

US transducers, particularly transceivers, convert the alternating current (AC) into the US wave and reverse. Each of these transducers has a large number of piezoelectric crystals embedded inside, namely elements. Depending on how US transducers excite these elements and how these elements are arranged, the transducers differ from each other. Among

Figure 1: Alpinion ultrasound device at Concordia University's PERFORM Centre for clinical and research purposes.

the currently existing transducers, linear transducers, convex transducers, and phase-array transducers are prevalent (Fig 2). In linear transducers, the elements are arranged linear and the shape of the beam is rectangular. Linear transducers have a fine near-field resolution typically. Convex transducers (curved transducers) have a curvilinear arrangement of the elements. They have fan-shaped beams and they are appropriate for in-depth examinations. Phased-array transducers are the most commonly used transducers. These transducers have an almost triangular beam shape and their beam, unlike the other transducers, can be moved and focused in different locations without moving the probe.

When the US transducers radiate the US wave, a percentage of waves influence the tissues and dissipate, while the rest of the US waves backscatter to the US transducer, namely echoes. The transducer process the echoes and make radio frequency (RF) lines and transfers them to the processor. By processing these RF lines, one can obtain distinct type of images. B-mode images or brightness images are 2D images that can be acquired by applying Hilbert transform on the RF lines. Fig. 3 demonstrates the B-mode image of a lamb's vertebra which was acquired with a curved transducer and the US machine shown

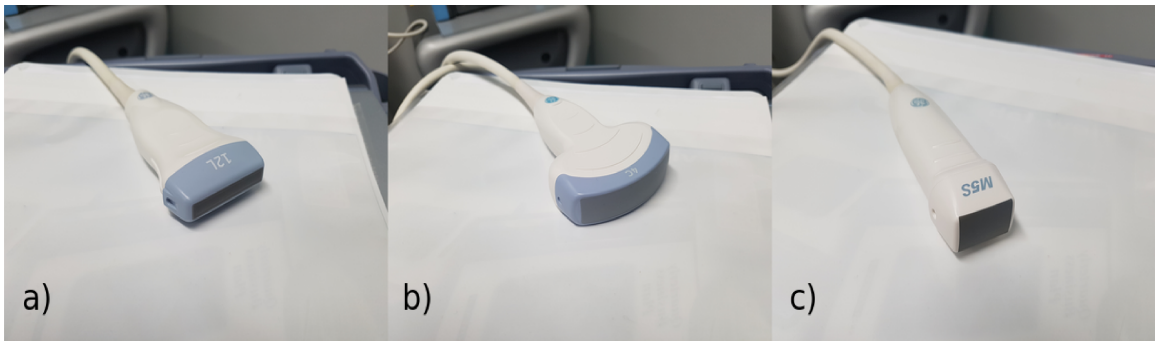

Figure 2: Most common US transducers: a) Linear b) Curved c) Phased-array.

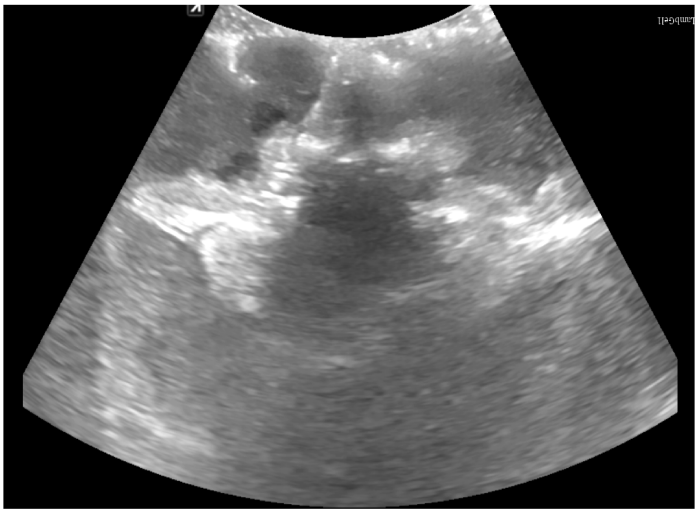

Figure 3: B-mode image of a lamb's vertebra which was collected with a curved transducer using an Alpinion ultrasound machine at the PERFORM Centre.

in the Fig. 1 at the PERFORM centre (Montreal, Canada).

Ultrasound imaging has a number of advantages that facilitates its usage in broad range of applications. The US equipment is widely available, inexpensive, non-invasive, and usually portable. Typically, the US images acquired with a high frequency transducer have higher resolution than most of the other medical imaging modalities. Also, US images display structures of organs and soft tissues very well. On the other hand, US imaging has disadvantages which restricts clinicians and researchers in some applications. US cannot penetrate the bone, therefore it is hard to image brain of adults. US images contain noise with artifacts. In some applications, such as intra-operative brain imaging, US offers poor visibility of structures so that surgeons require to acquire pre-operative MRI (or any

anatomical imaging) for achieving the desired accuracy in the surgery.

Nowadays, US imaging has an indispensible application in medicine. US imaging can be used in anesthesiology, angiology, cardiology, emergency medicine, gastroenterology, gynecology, musculoskeletal applications, and so forth. Wherein intra-operative US has great importance both in academic and clinical applications. Intra-operative US imaging in neurosurgery has been practised in many operation rooms and proved to be useful.

1.2 Image Registration

Image registration is the process of aligning two or more images [1]. The images are taken from a scene in different times and/or with different sensors and/or different viewpoints. Image registration is a fundamental image processing task in many applications such as remote sensing and medical imaging. Different sources of images offer a complementary information which is only possible after image alignments. Then, integration of information or image fusion will give the desired result. For example in remote sensing, the panchromatic grayscale image has a high resolution whereas the multispectral colored image offers a low resolution. Image fusion of these images would result in a colored high resolution image [2, 3, 4]. Moreover in medical imaging, fusion of the anatomical and functional images would give valuable information to the clinicians.

Image registration in medical imaging has been practiced for diagnosis purposes over the years. Different modalities in medical imaging were invented to be used for various medical objectives. Acquiring data of the same scene with different modalities and fusion of them gives clinicians and surgeons the desired information [5, 6, 7]. However, image registration may still fail, which is not acceptable in some medical applications. Therefore, automatic assessment of the quality of the image registration method is an active area of research [8]. One of the applications of image registartion in medical imaging is in image guided surgery (IGS). IGS systems can increase the accuracy of surgery [9, 10, 11]. IGS systems typically include an image registration technique to spatially align the pre-operative image to the intra-operative images. This procedure can assist the surgeons in

Figure 4: IGS system tracker at the PERFORM Centre. This system was set up to collect the experimental data of this thesis.

resection of tumors or estimation of the brain shift, and etc. Pre-operative anatomical images such as magnetic resonance imaging (MRI) and computed tomography (CT) are taken to facilitate the surgical planning with higher confidence. Amongst many modalites offered for intra-operative imaging, US imaging is worth to be taken into consideration. Fig. 4 shows the IGS system installed at the PERFORM Centre

Medical image registration techniques can be divided into various categories [12, 13, 14]. Image registration can be multimodal (registration of images with different modalities) [15, 16, 17, 18] or monomodal (registration of images with the same modality) [19, 20]. It can be manual, semi-automatic, or automatic which is executed without interaction of the operator. In terms of the algorithm, it can be feature-based or intensity-based. Feature-based applications extract features of the images or transform them to a different coordinate space instead of analyzing the image intensities directly. They have been employed for applications which the input images have large displacement with respect to each other. On the other hand, intensity-based image registration methods process the intensity of the images directly.

Intensity-based image registration techniques evaluate similarities of input images with a criterion in each stage. Moreover, they can employ a transformation to transform one image so that it aligns with the other image. Finally, by maximization of the similarity of images using the transformation parameters, the registration procedure is considered to be accomplished. Consequently, each intensity-based image registration technique can consist of a similarity metric, a transformation, and an optimizer [21].

The similarity metric can be as simple as calculating differences of corresponding pixels and then summating absolute or squared value of the differences which is defined as the sum of square differences (SSD). Literally, SSD assumes that two images after the registration would be the same. Obviously, SSD does not give good results for multimodal registrations. Correlation-based metrics offer more sophisticated relationship between images than SSD. Normalized cross-correlation (NCC) assumes that intensities of the images have a linear relationship with each other. One of the correlation-based similarity metrics is correlation ratio (CR) which assumes a functional relationship between intensities of the images. CR has been proposed in the context of medical image registration and used as a similarity metric in this application successfully [22, 23, 24]. The most general similarity metric can be mutual information (MI) which assumes no functional relationship between intensity of images. MI considers each pixel of the image as a random variable and derives a probability distribution function of the images. Then it calculates the similarity based on those probability distributions.

The transformation type is selected based upon the application [25]. When there is no deformation of the object scene, we can simply use a rigid transformation, which only has six degrees of freedom for 3D volumetric images. When one image has deformation with respect to the other one, transformations with more parameters can be used for instance, affine or free-form B-spline transformations. Affine transformation has 12 parameters and is collinear. So, if there are three or more points on the same line, they will be on the same line after the transformation and if there are two parallel lines, they will be parallel after the transformation. B-spline transformation consists of basis spline functions and it has multitude of parameters depending on the required accuracy. B-spline transformation can

compensate and estimate more complex non-linear deformations.

Among the current available optimization methods, gradient descent is a relatively simple optimization method in terms of the implementation. Gradient descent uses the first order derivative of the objective function, and therefore the convergence rate is relatively slow. Gradient descent zigzags for the non-convex and poorly defined convex functions. More importantly, estimation of the gradient is often computationally expensive. Therefore, stochastic gradient descent (SGD) optimization was invented to solve many problems related to the gradient descent. SGD proved to be a proper optimization algorithm for the problems where the analytic derivative of the objective function is available. In the image registration and image processing, mini-batch stochastic gradient descent (mBSGD) has more advantages over SGD. mBSGD is the refined version of SGD and instead of using only one random sample in each iteration, it uses N samples. There are many other optimization algorithms which were applied successfully to decrease the execution time such as Quasi-Newton (QN) optimization. One of the state-of-the-art optimization techniques is evolutionary strategies (ES). ES methods were proposed to optimize ill-posed black-box functions to increase the accuracy of optimization. ES methods are based on the evolution in genes of living creatures. Covariance matrix adaptation evolutionary strategy (CMA-ES) is one of the derivatives of these methods and was implemented in many medical image registration problems successfully [26].

1.3 Thesis Contributions

The contributions of this thesis are as follows:

- CR is used in small patches and calculated the similarity metric locally in Chapter 2 and 3. This makes our method insensitive to large variations in the intensity of ultrasound image caused by factors such as attenuation, shadowing and enhancement.
- For the first time it is shown that US and MRI images of the REtroSpective Evaluation of Cerebral Tumors (RESECT) database [27] can be automatically registered.

- The covariance matrix adaptation evolutionary strategy (CMA-ES) is used for the first time for registration of US and MRI and show that it works even for patients where a very large initial misalignment exists between US and MRI in Chapter 3.

- Three datasets were collected for validation of image registration techniques to register CT and US. These datasets are hard to collect and are therefore rare.

- A novel approach has been employed for above dataset to simulate the US images from their corresponding CT images. The dataset provides a gold standard ground-truth for image registration algorithms.

1.4 Thesis Outline

This thesis is organized as follows. In Chapter 2, MARCEL, an automatic image registration method that was proposed to register five patients of pre-operative MRI images of RESECT database to the intra-operative US images is proposed. In Chapter 3, we refined the method used in Chapter 2 and extended our method to apply it to all of the patients of the RESECT database. We acquired and distributed datasets of corresponding CT and US images to validate image registration of CT and US in Chapter 4. Finally, we provided avenues for future work and summarized this thesis in Chapter 5.

Chapter 2

MARCEL (inter-Modality Affine Registration with CorELation ratio): An Application for Brain Shift Correction in Ultrasound-Guided Brain Tumor Resection

This chapter has been published in the International MICCAI Brainlesion Workshop [28]. N. Masoumi, Y. Xiao, H. Rivaz, MARCEL (inter-Modality Affine Registration with CorELation ratio): An Application for Brain Shift Correction in Ultrasound-Guided Brain Tumor Resection, BrainLes MICCAI workshop, Springer, 2018, pp 55-63.

2.1 Introduction

Gliomas are tumors in glial cells occurring either in brain or spine, and are currently the most common types of brain tumors in adults [29]. According the world health organization (WHO), brain gliomas can be classified into four different grades: low grade (Grade I and II) and high-grade (Grade III and IV). Low-grade gliomas (LGG) have a slower tumor

growth rate, but will eventually progress to the deadlier high-grade tumors. Thus, early tumor removal can increase patient's survival rate [30].

During brain surgery, brain deforms to some extent, which is called brain shift and is caused by multiple reasons such as physiological factors [31]. Therefore, image guided neurosurgery systems (IGNS) that do not take brain shift into account can often render the pre-surgical plans invalid and can lead to incomplete or unnecessary resection.

Acquiring Magnetic Resonance Imaging (MRI) intra-operatively is difficult and requires special surgical tools and setups. Therefore, intra-operative ultrasound (US) has become popular due to its portability and non-invasiveness in recent years. The drawbacks with US are the low image quality and difficulty in interpreting the image contents. In order to track the surgical progress and brain shift, US images can be registered to pre-operative MRI to help recover the tissue deformation during operation [32]. Both T1-weighted MRI and T2-FLAIR MRI are rountinely acquired for planning brain tumor resection procedures. However, low-grade gliomas are often more distinguishable in T2-FLAIR than in T1-weighted MRI [27].

Intensity based registration techniques need a similarity metric to evaluate similarities between two images. In these techniques, the goal of the registration is maximization of the similarity metric. Among popular similarity metrics, mutual information (MI) is the most general one and assumes statistical relationship between images. On the contrary, normalized cross-correlation (NCC) and sum of squared differences (SSD) assume linear relationship between images and are more restrictive. Correlation ratio (CR) assumes functional relationship between images, and provides enough generality to be used as a similarity metric between US and MRI [26, 23, 33]. In [33] automatic multimodal deformable registration performed with utilization of a modified version of CR. They also proposed a robust method for dealing with resected tumor [34].

Deformable registration problems, usually have much more parameters than affine and rigid registration, which respectively have twelve and six parameters. As a result, they usually have more accurate registration. However, in practice, affine registration has a lower chance of failure and is generally less computationally intensive.

In this chapter, we introduced an automatic affine registration method using Robust paTch based cOrrelation Ration (RaPTOR) [33] to help recover brain shift using intra-operative US and pre-operative MRI scans. We used REtroSpective Evaluation of Cerebral Tumors (RESECT) database [27] to validate our method.

2.2 Materials and Methods

2.2.1 Registration Overview

Let I_f and I_m be respectively fixed and moving images. In the context of IGNS, we set I_f to the pre-operative MRI, and deform the intra-operative US image I_m towards the pre-operative MRI. We formulate the registration process as an optimization problem. Our cost C is defined in Eq. 1:

$$C = D(I_f(\mathbf{x}), I_m(\mathbf{T}(\mathbf{x}))) \tag{1}$$

where D is our objective function that should be minimized, I_f is the fixed image, I_m is the moving image, $\mathbf{x}$ is the point of interest in space, and $\mathbf{T}$ is the affine transformation matrix. The affine transformation matrix is defined in Eq. 2:

$$\boldsymbol{T} = \begin{bmatrix} a_1 & a_2 & a_3 & a_4 \\ a_5 & a_6 & a_7 & a_8 \\ a_9 & a_{10} & a_{11} & a_{12} \\ 0 & 0 & 0 & 1 \end{bmatrix} \tag{2}$$

where $a_i,\ 1 \leq i \leq 12$ denotes the twelve affine transformation parameters. If $\mathbf{x} = [x_i,\ x_j,\ x_k]$ denotes the position of a point in Cartesian coordinates, we employ the transformation as in Eq. 3:

$$\begin{bmatrix} y_i \\ y_j \\ y_k \\ 1 \end{bmatrix} = \boldsymbol{T}(\boldsymbol{x}) = \boldsymbol{T} \times \begin{bmatrix} x_i \\ x_j \\ x_k \\ 1 \end{bmatrix} \tag{3}$$

where $\mathbf{y} = [y_i,\ y_j,\ y_k]$ specifies the transformed point. We define the objective function D as a dissimilarity metric in Eq. 4. The dissimilarity metric is RaPTOR (Robust PaTch based cOrrelation Ratio), which is modified version of CR (Correlation Ratio) [33].

$$D(Y,X) = RaPTOR(X,Y) = \frac{1}{N_p}\sum_{i=1}^{N_p}(1-\eta(Y|X;\boldsymbol{\Omega_i})) \tag{4}$$

In Eq. 4, N_P is the number of patches, $\boldsymbol{\Omega_i}$ is the set of all voxels included in patch i, and η is CR. D varies between 0 and 1. In higher similarity, D is closer to 0 and in lower similarity D is closer to 1.

The definition of CR in Eq. 4 is as following:

$$1-\eta(Y|X) = \frac{1}{N\sigma^2}\left(\sum_{t=1}^{N} i_t^2 - \sum_{j=1}^{N_b} N_j\mu_j^2\right) \tag{5}$$

$$\mu_j = \frac{\sum_{t=1}^{N}\lambda_{t,j}i_t}{N_j}, N_j = \sum_t \lambda_{t,j} \tag{6}$$

where N is total number of samples in Y, $\sigma^2 = Var[Y]$, i_t is the intensity of voxel number t in Y, N_b is the total number of bins, and $\lambda_{t,j}$ is the contribution of sample t in bin j as explained in [33].

2.2.2 Optimization and Outlier Suppression

We calculated the derivation of objective function analytically in order to speed up the registration procedure. We used derivative of the cost function in two distinct part. First in outlier suppression part. Second in updating equation of the optimization part.

Derivative of the cost function with respect to affine transformation parameters is as following:

$$\frac{\partial D}{\partial \mathbf{a}} = \begin{bmatrix}\frac{\partial D}{\partial a_1} & \frac{\partial D}{\partial a_2} & \dots & \frac{\partial D}{\partial a_{12}}\end{bmatrix}^T \tag{7}$$

In Eq. 7, $\mathbf{a}$ is a vector consisting of affine transformation parameters. Now the derivative with respect to each of the parameters is:

$$\frac{\partial D}{\partial a_k} = \frac{1}{N_p}\sum_{i=1}^{N_p}\frac{\partial(1-\eta(Y|X;\boldsymbol{\Omega_i}))}{\partial a_k} \tag{8}$$

where $a_k,\ 1 \leq k \leq 12$ declares affine transformation parameters. Utilizing the chain rule, we have:

$$\frac{\partial(1-\eta(Y|X;\mathbf{\Omega_i}))}{\partial a_k} = \frac{\partial(1-\eta)}{\partial a_k} = \frac{\partial(1-\eta)}{\partial I_m(\mathbf{T}(\mathbf{x}))}.\frac{I_m(\mathbf{T}(\mathbf{x}))}{\partial \mathbf{d}}.\frac{\partial \mathbf{d}}{\partial a_k} \tag{9}$$

where $\mathbf{d} = [d_x, d_y, d_z]$ in Eq. 9 is the displacement vector in Cartesian coordinates. Right hand side of Eq. 9 has three terms. The first term was calculated in [33]. In order to comply with our equations, we bring up the calculation in following equations. Note that the first term in Eq. 9 is the size of transformed moving image and we consider each element of this term as in Eq. 10 using Eq. 5.

$$\begin{gathered}\frac{\partial(1-\eta)}{\partial i_t} = \frac{\partial}{\partial i_t}\left(\frac{1}{N\sigma^2}\left(\sum_{k=1}^{N} i_k^2 - \sum_{j=1}^{N_b} N_j\mu_j^2\right)\right) = \\ \frac{-2(N-1)}{N^3\sigma^4}(i_t-\mu)\left(\sum_{k=1}^{N} i_k^2 - \sum_{j=1}^{N_b} N_j\mu_j^2\right) + \\ 2(i_t - \sum_{j=1}^{N_b}\mu_j\lambda_{t,j})(\frac{1}{N\sigma^2})\end{gathered} \tag{10}$$

In Eq. 10 μ is mean of Y. Second term in right hand side of Eq. 9 is simply the gradient of transformed moving image and third term is Jacobian of transformation.

Mini-Batch Gradient Descent Optimization: While batch gradient descent is time consuming and stochastic gradient descent (SGD) doesn't have required accuracy, choice of mini-batch gradient descent gives a trade-off between implementation time and result accuracy. For a certain resolution of input images, we select a set of random patches from the images in every iteration.

We employ Gaussian pyramid in the optimization. There are three pyramid levels in our analysis excluding the original size of images. In order to enable the dissimilarity metric to have a better perception of similarities between two input images, we select the set size of patches proportional to the resolution and size of input images in each level. Note that increasing the set size of patches will increase the computation time. Thus selecting the set size of patches in each pyramid level is a compromise between accuracy and computation time. The update equation for mini-batch gradient descent is as Eq. 11:

$$\boldsymbol{a_n} = \boldsymbol{a_{n-1}} - \alpha_n \frac{\partial D}{\partial \boldsymbol{a_{n-1}}} \tag{11}$$

where a_n is the vector consisting of affine transformation parameters in n-th iteration, $\frac{\partial D}{\partial \boldsymbol{a_n}}$ can be achieved by Eq. 7, and α_n is step size. Step size is a function of iteration number and is defined in Eq. 12.

$$\alpha_n = \frac{a}{(A+n)^\tau} \tag{12}$$

In Eq. 12 $a > 0$, $A \geq 0$, $0 < \tau \leq 1$ are constants. Klein et. al. [26] suggested approximate values for these parameters. According to [26], we set $a = 0.001$, $A = 0.3 \times MaxIterations$, and $\tau = 0.65$.

In comparison to the MRI, US has quite unique image features and its own challenges. The inherent properties of the ultrasound images can have a major effect on performance of the dissimilarity metric. Since we select patches in each iteration randomly, before any operation on the selected patches, we should pre-select the patches that have potent image features (e.g., consistent and strong lines). We used outlier suppression proposed in [33]. We discard patches that are greater than a threshold T in Eq. 13.

$$r.r_g > T \tag{13}$$

Heuristically, $T = 1$ gives acceptable results for us. Parameter r is defined in Eq. 14.

$$r = min\left\{ \frac{Var(\frac{\partial D}{\partial d_x})}{\langle \frac{\partial D}{\partial d_x} \rangle^2}, \frac{Var(\frac{\partial D}{\partial d_y})}{\langle \frac{\partial D}{\partial d_y} \rangle^2}, \frac{Var(\frac{\partial D}{\partial d_z})}{\langle \frac{\partial D}{\partial d_z} \rangle^2} \right\} \tag{14}$$

where $\frac{\partial D}{\partial d_x}$, $\frac{\partial D}{\partial d_y}$, and $\frac{\partial D}{\partial d_z}$ are derivatives in x, y, and z direction respectively and $\langle . \rangle$ is mean operator. The denominators are low at relatively uniform regions, but are high in textured regions (i.e., with high gradients). Definition of r_g in Eq. 13 can be found in Eq. 15.

$$r_g = \frac{\|\nabla I_f\| * B}{\|\nabla I_m\| * B} \tag{15}$$

Here ∇ is gradient operator, $\|.\|$ indicates magnitude of the gradient, $*$ is convolution, and B is a kernel of size of the image with all ones in the selected patch and zeros the rest. The nominator and denominator represent summation of gradient values of fixed and moving image respectively.

2.2.3 Patient Data

To validate the proposed technique, we employed the MRI and intra-operative US scans of five patients, who underwent brain tumor resection procedures. All patients' data were randomly selected from the publicly available RESECT (REtroSpective Evaluation of Cerebral Tumors) database [27], which includes both pre-operative MRI and intra-operative US scans of patients with low-grade gliomas, as well as homologous anatomical landmarks for validating registration algorithms. For registration, we employed T2w FLAIR MR images, which better visualize the boundaries of the brain tumors than the T1w MR scans, and intra-operative US scans obtained before resection. The T2w FLAIR images (TE=388ms, TR=5000 ms, flip angle=120 deg., voxel size=1x1x1 mm^3, sagittal acqusition) were obtained one day before surgery on a 3T Magnetom Skyra (Siemens, Erlangen). The MRI volumes have been rigidly registered to the patient's anatomy on the surgical table. The spatially tracked US images were obtained with a sonowand Invite neuronavigation system (Sonowand AS, Trondheim, Norway), and then reconstructed as 3D volumes with resolutions range from 0.14x0.14x0.14 mm^3 to 0.24x0.24x0.24 mm^3 depending on the transducer types and imaging depths. All US volumes have full coverage of the tumors. Since the US volumes were spatially tracked during surgeries, the positions of the tissues truthfully reflect the tissue formation during the procedures. Corresponding anatomical landmarks between the MRI and US volumes were provided in the dataset for registration validation.

2.2.4 Registration Procedure

For each patient, we first up-sampled the MR image to the image space (and resolution) of the corresponding US images. Then, the US volumes were registered to the re-sampled MRI volumes using the technique introduced earlier. For our registration, we used a hierarchical approach, which facilitate the optimization efficiency. The registration results are reported as mean target registration errors (mTREs) for all patients under study.

Table 1: mTRE before and after registration

Patients No.	Initial mTRE	Final mTRE	No. of Landmarks
1	5.72	2.86	15
2	9.58	3.21	15
3	2.65	1.79	15
4	4.70	2.14	15
5	2.99	1.62	15
mean	5.13	2.32	
std	2.78	0.68	

2.2.5 Validation

In order to assess the accuracy of our method, we used the landmarks which were provided in RESECT database for each patient. Supplied landmarks can be used to calculate mean target registration error (mTRE) [35]. mTRE for a patient is defined as Eq. 16.

$$mTRE = \frac{1}{N}\sum_{i=1}^{N} \|\boldsymbol{T}(\boldsymbol{x_i}) - \boldsymbol{x_i'}\| \tag{16}$$

Where $\boldsymbol{x_i}$ and $\boldsymbol{x_i'}$ are two corresponding landmarks in moving image (US in our case) and fixed image respectively. In Eq. 16, N is the total number of landmarks.

2.3 Results

After image registration, we have observed an improvement in terms of image feature correspondence. From Fig. 5 and 6, we can see that borders of tumors (blue arrows) and sulci (green arrows) have been visibly re-aligned between the MR and US images. The detailed mTRE evaluation for each patient is shown in Table 1. Figure 7 depicts mTRE values before and after registration as well. Both in Table 1 and Fig. 7, we observe that mTRE values decreased after registration. Moreover, it is instructive to compare mean and standard deviation of mTRE values before registration with ones after registration. In Table 1, we can see not only the mean value but also the standard deviation decreased.

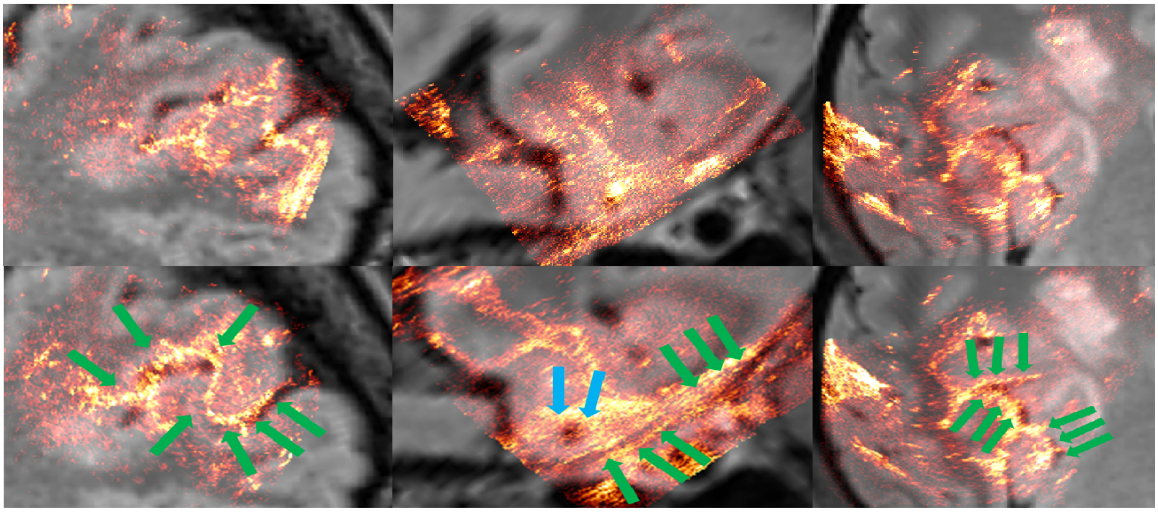

Figure 5: Overlay of MR and US before and after registration for patient one, two, and three. First row is before registration and second row is after registration. Patient one, two, and three are first, second, and third column respectively. Green arrows correspond to sulcus and blue arrows correspond to tumor borders.

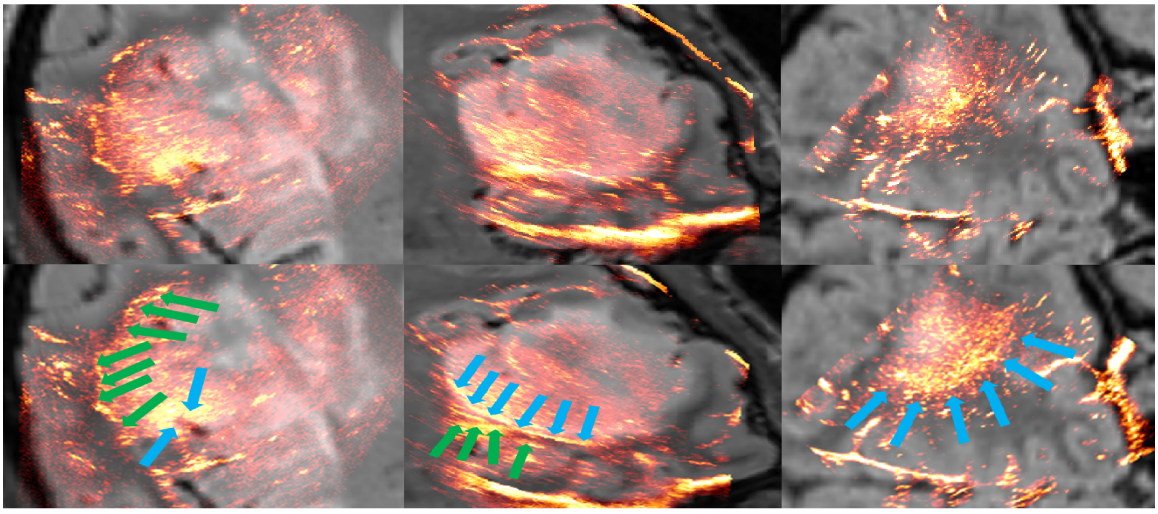

Figure 6: Overlay of MR and US before and after registration for another view of patient three, four, and five. First row is before registration and second row is after registration. Patient three, four, and five are first, second, and third column respectively. Green arrows correspond to sulcus and blue arrows correspond to tumor borders.

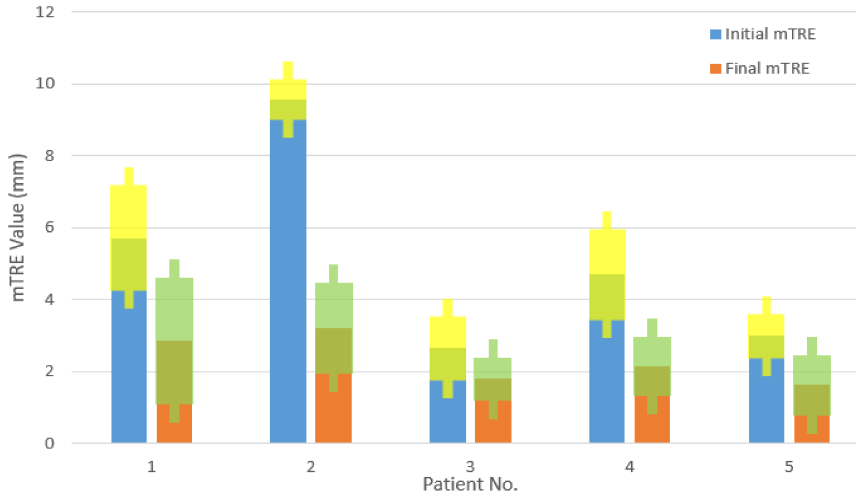

Figure 7: Mean Target Registration Error (mTRE) Before and After Registration. Yellow and green bars indicate standard deviation before and after registration respectively.

2.4 Discussion

Although an affine transformation has much fewer parameters than a non-linear deformation, and thus may not fully represent the underlying soft tissue deformation, a few reasons justify the use of affine transformation for the demonstrated application. First, affine registration is often faster and less prone to failure than nonlinear registration. Second, the US volumes used in this chapter mainly cover the tumorous tissues, and thus the deformation can be approximated sufficiently well locally with affine transformation. Lastly, the tissue deformation before resection is not severe, and affine registration may be sufficient for the surgeons to navigate the surgical plans.

2.5 Conclusion

We have proposed an automatic affine registration method based on correlation ratio. The technique has been demonstrated retrospectively for MRI-US registration in the context of brain shift correction during low-grade brain gliomas resection. From both quantitative and qualitative assessments, our proposed method has shown to successfully realigned the intra-operative US with the pre-operative MRI scans.

Chapter 3

ARENA: Inter-modality affine registration using evolutionary strategy

The method proposed in the previous chapter could not improve the image alignments for all patients in the RESECT dataset. In this chapter, we propose a method using a new optimization algorithm to staisfy clinical requirements of the image alignments for all the patients.

The material in this chapter has been submitted as:
N. Masoumi, Y. Xiao, H. Rivaz, ARENA: Inter-modality affine registration using evolutionary strategy, International Journal of Computer Assisted Radiology and Surgery, Springer, 2018.

3.1 Introduction

In medical imaging, we often have chronological images of tissues (which are usually collected with different imaging modalities) that need to be aligned [36, 37]. Fusion of the information of those corresponding images is proven to provide useful information to clinicians [5, 38, 39]. Even though registration based on manually selected homologous

landmarks can be performed on images, the corresponding images are often misaligned due to reasons such as tissue deformation and errors in landmark selection. For example, in image-guided surgery, deformation of the organs, such as the brain can invalidate surgical plannings [9, 40, 41, 31].

Image registration is the method, which aligns corresponding misaligned images acquired in different times and/or with different sensors [42]. One can categorize image registration methods in various classes such as automatic or with interaction with the user [43]. Automatic image registration is generally faster and avoids erroneous actions of the user [44]. Another classification can be made based on the method used: intensity-based or feature-based. Intensity-based image registration methods generally work better for smaller deformations, whereas feature-based methods generally work better if the initial misalignment is large [45, 1].

An automatic intensity-based image registration method can consist of different components. One image would be chosen as the template or fixed image (I_f). The other image is called the moving image (I_m). During the registration process, I_m should move to be registered to I_f. The movement of I_m can be restricted and modeled by a spatial transformation. A transformation type is selected based upon the application [46, 47, 48]. When there is no deformation of the object scene, we can simply use a rigid transformation, which only has six degrees of freedom [49, 50, 51]. When one image has deformation with respect to the other one, we can use transformations with more parameters for instance, affine or free-form B-spline transformations [52, 53, 54]. The image registration method should have a similarity metric to evaluate the similarity of two images after the transformation. On one end of the spectrum, the similarity metric can assume a restrictive equality relationship between image intensities and easily subtract two images as in sum of square differences (SSD). On the other end of the spectrum, it can assume a general information-based similarity between images as in mutual information (MI) [55]. Correlation ratio (CR) assumes a functional relationship between intensities of the two images and provides a compromise between these two extremes. The third component of registration methods, maximizes the similarity of the images by varying the parameters of the chosen

transformation [23, 24, 22].

We proposed an automatic intensity-based image registration method using the refined version of CR. The proposed method is an extended version of the method proposed in [28] which was itself based on RaPTOR (Robust PaTch-based cOrrelation Ratio) [33]. Our similarity metric measures similarity of the images based on corresponding patches locally. We modeled movement of I_m with affine transformation and used covariance matrix adaptation evolutionary strategy (CMA-ES) [56] as the optimization approach. We applied our method on RESECT (REtroSpective Evaluation of Cerebral Tumors) database [27] to validate the results. Recent work has successfully performed US-US registration of the RESECT database [57]. To the best of our knowledge, no previous work has tackled US-MRI registration in this database.

This chapter is organized as follows. In Section 3.2, we elaborate our method and derive the equations. In Section 3.3, qualitative and quantitative validation of the method are presented. In Section 3.4, we discuss the advantages and disadvantages of our method and avenues for the future. And finally, we provide a brief conclusion in Section 3.5.

3.2 Methods

Let I_m and I_f be respectively the moving and fixed images. In our registration problem we fix I_f and move I_m so that it matches I_f. We transform I_m with $\mathbf{T}$. The optimal $\mathbf{T}$, when applied to I_m, for each point like $\mathbf{x}$ in the space of images, gives us the best alignment of I_f and I_m. Alignment of I_f and I_m is measured by a dissimilarity metric D. The best alignment of I_f and I_m with T corresponds to minimum achievable D. In other words, our goal is to minimize the following cost function:

$$C = D(I_f(\mathbf{x}), I_m(\mathbf{T}(\mathbf{x}))) + R(\mathbf{T}) \tag{17}$$

where $R(\mathbf{T})$ is a regularization term to enforce a smooth transformation and C is the cost function. Minimizing C by varying $\mathbf{T}$ provides the transformation that aligns the fixed and moving images.

3.2.1 Dissimilarity Metric

As explained in Eq. 17, D measures the alignment of input images i.e. the fixed and moving images. Since CR is an asymmetric similarity metric, the order of computing CR is important. To allow either I_m or I_f to be the first or second image in CR, we label our input images as X and Y. D in Eq. 17 and in Eq. 18 is the amended version of RaPTOR [33]. D can vary from zero to one. In case that X and Y are the same, $D = 0$. When X and Y do not have any similarity, $D = 1$. Therefore D is a dissimilarity metric. In Eq. 18, η is CR, the similarity metric proposed by Roche et al [23]. The similarity metric needs to identify corresponding features of X and Y locally. Because our goal is to simulate human perception with a similarity metric and human perception identifies two images aligned when one founds out that features or landmarks are aligned locally. So we calculate CR in N_P corresponding pacthes of X and Y.

$$D(Y, X) = \frac{1}{N_p} \sum_{i=1}^{N_p} (1 - \eta(Y|X; \boldsymbol{\Omega_i})) \tag{18}$$

where $\boldsymbol{\Omega_i}$ reperesents the patch i space. The definition of CR in Eq. 18 is as following:

$$1 - \eta(Y|X) = \frac{1}{N\sigma^2} \left(\sum_{t=1}^{N} i_t^2 - \sum_{j=1}^{N_b} N_j \mu_j^2 \right) \tag{19}$$

$$\mu_j = \frac{\sum_{t=1}^{N} \lambda_{t,j} i_t}{N_j}, N_j = \sum_t \lambda_{t,j} \tag{20}$$

where N is the total number of voxels in Y, $\sigma^2 = Var[Y]$, i_t is the intensity of voxel number t in Y, N_b is the total number of bins, and $\lambda_{t,j}$ is the contribution of sample t in bin j as proposed in [33].

Obviously in calculation of D in Eq. 18, pacthes that have approximately the same voxel intensities or equally small variances, should be discarded because they do not include any image feature. Therefore, we apply a gamma correction on patches of X and Y as the one explained in [58] after selecting patches in X and Y to increase variance of patch intensities. We normalize intensities of the patches right after the gamma correction. Then every pair of patches in which $\sigma^2 < T$ are discarded. Heuristically, we found that $T = 1$ is the best value.

3.2.2 Transformation

We used affine transformation to model the movement of moving image. Unlike non-linear transformations, affine transformation cannot fold or rupture the tissue. Therefore, we found out that no regularization is needed in the cost function of Eq. 17. The affine transformation matrix is defined as:

$$\boldsymbol{T} = \begin{bmatrix} a_1 & a_2 & a_3 & a_4 \\ a_5 & a_6 & a_7 & a_8 \\ a_9 & a_{10} & a_{11} & a_{12} \\ 0 & 0 & 0 & 1 \end{bmatrix} \tag{21}$$

As one can see in Eq. 21, the affine transformation has twelve parameters which are a_i, $1 \leq i \leq 12$. In general, these twelve parameters can be any real number.

Consider a point in the cartesian coordinate as $\mathbf{x} = [x_i,\ x_j,\ x_k]$. This point can be transformed by the affine transformation as in Eq. 22:

$$\begin{bmatrix} y_i \\ y_j \\ y_k \\ 1 \end{bmatrix} = \boldsymbol{T}(\boldsymbol{x}) = \boldsymbol{T} \times \begin{bmatrix} x_i \\ x_j \\ x_k \\ 1 \end{bmatrix} \tag{22}$$

where $\mathbf{y} = [y_i,\ y_j,\ y_k]$ is the transformed point in the cartesian coordinate.

3.2.3 Optimization

The explanation in the Section 3.2 defines the registration procedure as an optimization problem. Image registration, in general, is an ill-posed problem, and consequently entails optimizing a highly non-convex objective function [59]. In order to tackle this problem, we deployed CMA-ES as our optimizer. In Eq. 17, C is the cost of the objective function D. The affine transformation parameters a_i, $1 \leq i \leq 12$ in Eq. 21 are used by the optimization algorithm to minimize C in Eq. 17.

CMA-ES is similar to natural selection of the biological creatures [60]. In each iteration

(generation) λ new candidate solutions (offsprings) $x_k^{(g+1)},\ 1 \leq k \leq \lambda$ are calculated from the best μ out of λ of the last generation (parents) $x_{i:\lambda}^{(g)},\ 1 \leq i \leq \mu$.

There are $N = 12$ degrees of freedom in the optimization established by affine transformation parameters. Hence, the parameter settings for λ and μ are $\lambda = 4 + \lfloor 3\ln(N) \rfloor$ and $\mu = \lfloor \lambda/2 \rfloor$. CMA-ES update equation for the generation g to $g+1$ is presented in Eq. 23.

$$x_k^{(g+1)} = \frac{1}{\sum_{i=1}^{\mu} w_i} \sum_{i=1}^{\mu} w_i x_{i:\lambda}^{(g)} + \sigma^{(g)} \boldsymbol{B}^{(g)} \boldsymbol{D}^{(g)} z_k^{(g+1)} \tag{23}$$

where $w_i, 1 \leq i \leq \mu$ are summation weights of offsprings and they are calculated as Eq. 24.

$$w_i = \ln(\frac{\lambda+1}{2}) - \ln(i) \tag{24}$$

In Eq. 23 $\sigma^{(g)} \in \mathbb{R}^+$ is the step size at the generation g. So called covariance matrix $\boldsymbol{C^{(g)}}$ in the generation g is a symmetric positice definite $N \times N$ and its relationship with defined parameters is presented in Eq. 25:

$$\boldsymbol{B}^{(g)} \boldsymbol{D}^{(g)} z_k^{(g+1)} \sim \mathcal{N}(\mathbf{0}, \boldsymbol{C^{(g)}}) \tag{25}$$

For detailed explanations and equations of $\sigma^{(g)}$, $\boldsymbol{B}^{(g)}$, $\boldsymbol{D}^{(g)}$, $z_k^{(g+1)}$, and $\boldsymbol{C^{(g)}}$ one can refer to [60].

3.2.4 Patient Data

We applied the proposed image registration method on the RESECT database [27]. The RESECT database is an open source clinical database that contains 23 surgical cases of low-grade gliomas resection operated at St. Olavs University Hospital. With the primary goal to help develop image processing techniques for brain shift correction, for each patient, the dataset provides pre-operative T1w and T2-FLAIR MRI scans, intra-operative 3D ultrasound volumes obtained before, during, and after tumor resection, and corresponding anatomical landmarks between MRI-US pairs and US-US pairs. To demonstrate our proposed algorithm, we used the pre-operative T2-FLAIR MRI and US volume before tumor resection since often this stage sets the tone for the total brain shift after craniotomy.

More specifically, 22 patients from the RESECT dataset were used, where 15-16 pairs of MRI-US homologous landmarks were manually tagged.

3.2.5 Registration Procedure

For each patient, we first up-sampled the MRI image (resolution $= 1 \times 1 \times 1mm^3$) to the resolution of corresponding US image because of the US images considerable higher resolution (resolution $= 0.24 \times 0.24 \times 0.24mm^3$). Then we implemented the image registration algorithm on each patient. For better performance of our method, we used up to four levels of Gaussian pyramids to tackle the large misalignment present in some of the cases.

3.3 Results

3.3.1 Qualitative Validation

By comparing the images before and after the registration, with visual inspection, we evaluated quality of the registration. We compared alignment of corresponding brain anatomical features for instance sulci and tumor boundaries in the MRI and US images before and after registration. Each patient data includes the brain tumor in MRI and US images. We checked whether alignment of the boundary of the tumor has been improved as well. Figure 8 demonstrates overlaid US on MRI of Patient 12. The first column shows the slices before registration while the second column shows the slices after the registration. First row is axial view, second row is sagittal view, and the last row is coronal view. The arrows show where the registration had improvements. The tumor has a brighter color in both MRI and US image. As it is clear from this figure, registration improved alignment of the tumor boundary and sulci.

Figure 9 shows overlaid US and MRI slices of sagittal view for Patient 5, 19, and 21 in RESECT database [27]. Columns show before and after the registration respectively. Each row corresponds to an individual patient. The arrows guide the reader to locate the improvement after the registration. The first row shows a significant improvement in tumor

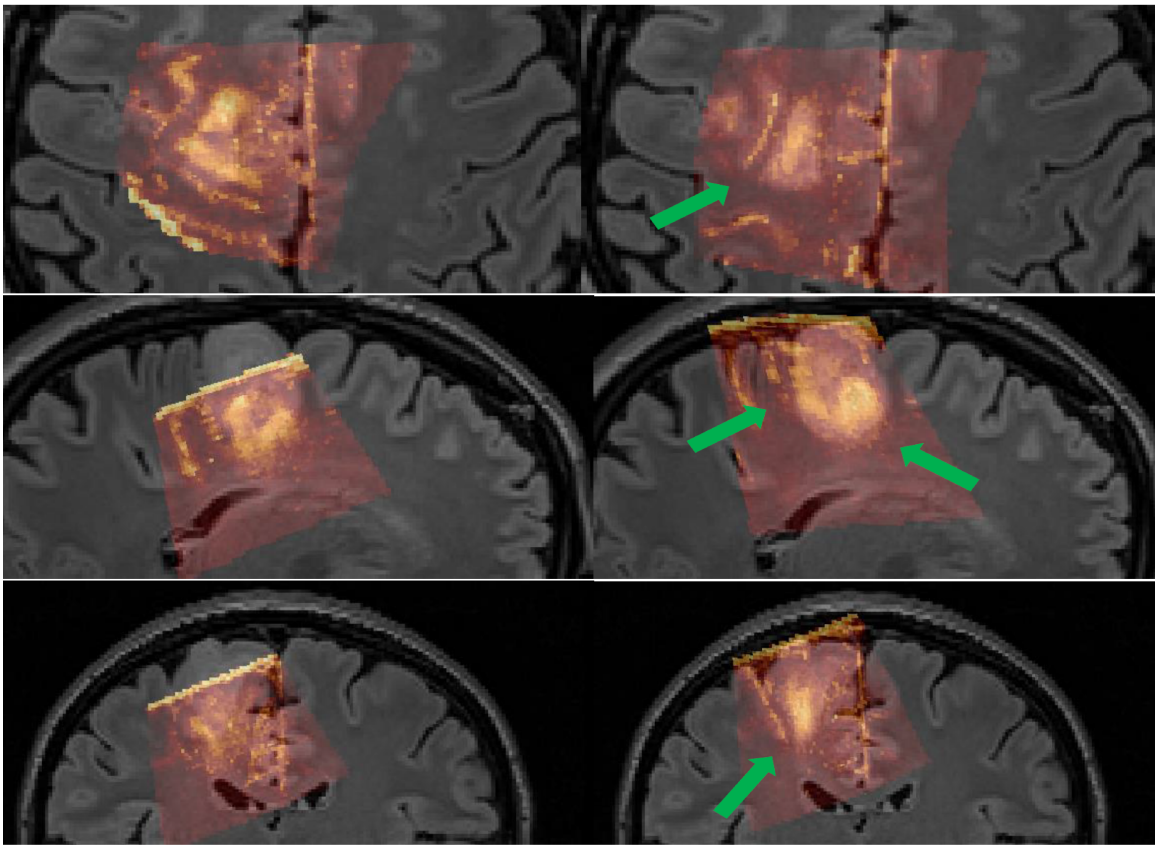

Figure 8: Demonstration of US overlaid on MRI for Patient 12. Columns show before and after registration and rows show axial, sagittal, coronal view respectively. The arrows show where the images had improvements.

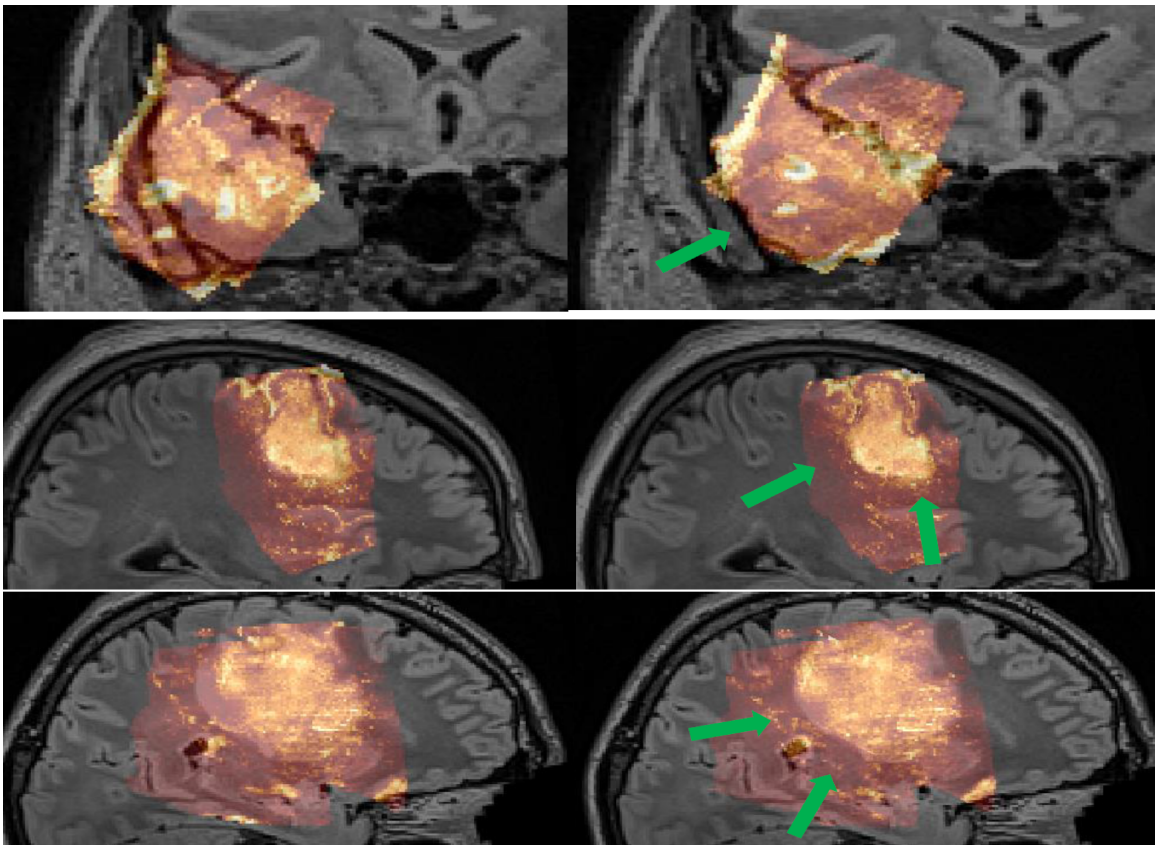

Figure 9: From the top row, sagittal view of Patient 5, 19, and 21 respectively. Columns show before and after the registration respectively. The arrows show where the images had improvements.

and sulci region. The second and the third rows show improvements around the tumor region.

3.3.2 Quantitative Validation

Corresponding homologous landmarks are selected manually in the US and MRI in the RESECT database by two experts. Consider N as the total number of corresponding landmarks in US and MRI volumetric images. We used the provided landmarks to calculate mean target registration error (mTRE) [35]. mTRE for each patient is defined as Eq. 26:

$$mTRE = \frac{1}{N}\sum_{i=1}^{N} \|\boldsymbol{T}(\boldsymbol{x_i}) - \boldsymbol{x'_i}\| \tag{26}$$

where $\boldsymbol{T}$ is the optimal affine transformation derived after implementing the image registration algorithm.

Initial mTRE of each patient before registration and the number of landmarks for each patient is demonstrated in Table 2. Each patient has N landmarks and affine transformation has twelve parameters. In this table, minimum achievable mTRE is the minimum mTRE we can achieve using an affine transformation for the registration. We made system of linear equations to find the optimal achievable affine transformation. In this system , the provided landmarks are knowns and the optimal affine transformation parameters are unknowns. Therefore, the number of knowns is more than the number of unknowns $N > 12$. We solved this overdetermined problem with least squares (LS). We reported LS solution for each patient in Table 2. It is worth mentioning that the minimum achievable mTREs are calculated the similar way as the fiducial registration error (FRE) [61], they are not equal to FRE. FRE is the root mean square error (RMSE) and we calculate mean root square error (MRSE) so that it can be compared to the initial and final mTRE values calculated before and after registration respectively.

We compared our method with the one introduced in [33]. The registration is an automatic deformable registration in MRI-US application. They used RaPTOR as a similarity metric, free form B-spline transformation, and stochastic gradient descent optimization. The comparison is shown in Table 3.

Our method improved alignments for each patient. The overall performance of our method is better than RaPTOR in terms of mean value and standard deviation of mTRE. RaPTOR has failed to improve mTRE for some patients especially for patients with higher initial mTRE. In Table 2, initial mTRE shows rather high value of standard deviation. As in Table 3, our method had a significant improvement for standard deviation. One can interpret it as ability of the method to improve a wide range of misaligned images with high mTRE values. Figure 10 shows the data in Table 2 and Table 3 in one chart.

In addition to the validation method, we did a statistical analysis of our results. We used the Wilcoxon rank sum test which is a nonparametric statistical analysis method [62]. In this test, the null hypothesis H_0 is: the method did not have improvement in mTRE. Using

Table 2: RESECT database initial mTRE of patients, minimum achievable mTRE by affine transformation, and number of landmarks

Patients ID No.	Initial mTRE (mm)	Minimum Achievable mTRE (mm)	No. of Landmarks
1	1.82	1.1	15
2	5.72	1.11	15
3	9.58	0.8	15
4	2.98	0.95	15
5	12.16	0.93	15
6	3.32	0.75	15
7	1.88	1.22	15
8	2.65	1.08	15
12	19.71	0.91	16
13	4.7	0.9	15
14	3.00	0.89	15
15	3.36	1.33	15
16	3.41	0.91	15
17	6.4	1.03	16
18	3.64	0.78	16
19	3.16	0.86	16
21	4.44	0.68	16
23	7.04	0.69	15
24	1.11	0.7	16
25	10.08	0.87	15
26	2.91	0.98	16
27	5.82	1.03	16
Mean(μ)	5.40	0.93	-
Std(σ)	4.28	0.17	-

Table 3: Comparison of ARENA against RaPTOR

Patients ID No.	RaPTOR (mm)	ARENA (mm)
1	1.73	1.49
2	4.48	3.23
3	5.1	3.65
4	2.88	2.04
5	12.21	4.08
6	3.33	1.55
7	1.84	1.7
8	1.73	1.76
12	19.76	5.52
13	4.75	2.92
14	2.95	2.61
15	1.77	2.46
16	3.37	1.63
17	2.53	3.69
18	1.12	1.96
19	2.09	2.66
21	1.27	3.08
23	5.66	3.15
24	1.25	1.04
25	10.07	4.56
26	1.44	2.5
27	3.94	3.99
Mean(μ)	4.33	2.79
Std(σ)	4.44	1.13

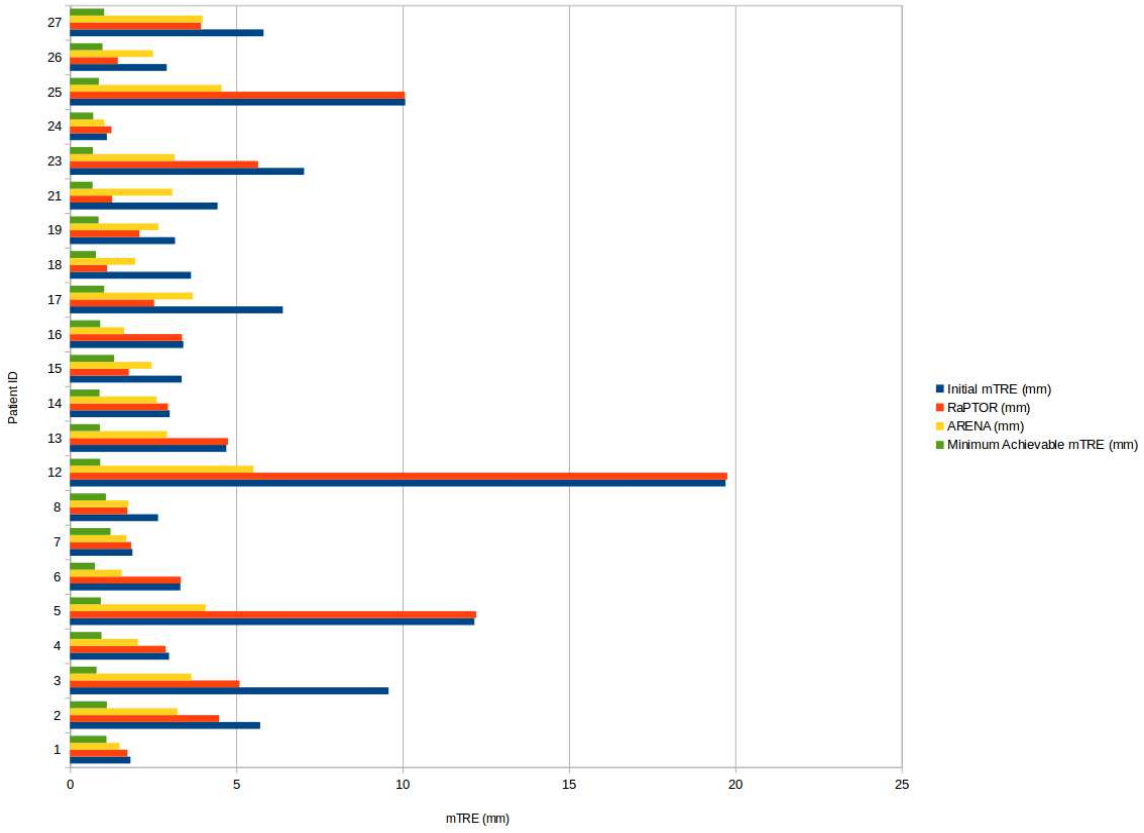

Figure 10: Initial mTRE (mm), RaPTOR results (mm), ARENA results (mm), and minimum achievable mTRE (mm) with affine transformation.

the data in Table 2, the null hypothesis is $\mu = 5.40$. The alternative hypothesis H_1 would be $\mu \geqslant 5.40$. Using the initial mTRE before the image registration and the results in Table 3, we achieved the p-value of 0.0058 by applying Wilcoxon rank sum test. Considering the conventional significance level of $\alpha = 0.05$, $p = 0.0058$ shows that not only we reject H_0 and H_1, but also with $\%99.42$ confidence we improved the result.

3.4 Discussion

We showed the minimum achievable mTRE values with an affine transformation to provide a lower bound for mTRE values. We have not used these values to optimize and improve ARENA. We achieved mTRE values that are very close to this minimum value in some patients (e.g. Patient 24). However, the average minimum achievable mTRE is 0.93mm, which is smaller than the accuracy of the landmark selection. Therefore, it is expected that our final mTRE values be larger than the minimum achievable error.

In this work, we proposed to use a simple affine transformation to correct for brain shift. Nevertheless, non-linear transformations offer more flexibility and allow us to recover the deformation more accurately. Before employing affine transformation we used simple translation, rigid transformation, and rigid transformation with scaling parameters. We notice that none of them are able to improve mTRE for all patients. Affine transformation was the least general transformation model that could give us significant improvement in mTRE. Affine transformation is simpler and faster than non-linear transformations, and practical in a wide range of applications.

CR and its derivatives RaPTOR and ARENA are asymmetric similarity metrics, meaning that reversing the order of images changes the similarity value and likely the results. We set the US and MRI as moving and fixed images respectively since this provided better results for ARENA. Since ARENA uses affine transformation, it can be simply inverted if clinicians prefer to deform the MRI to align with US.

Image registration with affine transformation has a good performance for structural images. But for functional data, such as tractography, nonlinear deformation is necessary to

preserve the continuity of the tracts [63]. We investigated further the reason why RaPTOR failed to improve the mTRE in some patients. We tried to initialize RaPTOR with a rigid registration and modify the tunable parameters. After that the performance of RaPTOR substantially improved. In contrast, ARENA does not need to be initialized with a rigid registration and works even for cases with large misalignment.

3.5 Conclusion

Herein, we presented ARENA, an affine registration method to align US and MRI volumetric images. We applied our method on RESECT dataset and validated our method qualitatively and quantitatively. The qualitative results show that the registered images have improvements in alignment of salient image features. We compared our method with RaPTOR which is a deformable state-of-the-art image registration method. Our method had overall advantage over RaPTOR especially in patients with higher initial mTRE wherein RaPTOR provided minimal improvements in mTRE. ARENA has consistently improved the mTRE in all patients, and is therefore a potentially promising registration method for use during IGNS.

Chapter 4

Datasets to validate image registration for computed tomography and ultrasound of vertebrae

The material in this chapter outlines methods and results in creation of a database of ultrasound (US) and computed tomography (CT) images that can be used for validation of US-CT registration techniques.

4.1 Data

The described data consists of three datasets. The first one is 3D simulated US scans of two human patients lumbar vertebrae from their respective publicly available CT images [64, 65]. For Patients 1 and 2, we included the L2 lumbar vertebra and the L1 lumbar vertebra respectively. The second dataset is the CT scan and the spatially tracked US of a post-mortem canine vertebrae, namely the phantom. The phantom consists of 2 cervical and 8 thoracic canine vertebrae. The CT and US images were acquired in such a way that 2 cervical and 2 thoracic vertebrae are included in the images. The third dataset is the lambs lumbar vertebraes CT and US image set. The CT image contains 5 lumbar vertebrae and in the US image of the lumbar vertebrae L2 to L5 are included. For the second and the third

datasets, we found 15 homologous landmarks in the CT and US images which were tagged manually.

4.2 Experimental Design, Materials, and Methods

4.2.1 Simulated US

We employed CT images provided by The Cancer Genome Atlas Sarcoma (TCGA-SARC) [64, 65]. Patients were imaged with the CT scanner (GE LightSpeed VCT) using the protocol 5.7 CAP STANDARD-3CC/SEC. The axial slices had a thickness of $5.00mm$ and an in-slice resolution of $0.74 \times 0.74mm^2$. We extracted the L2 lumbar vertebra of the Patient TCGA-QQ-ASV2 and L1 vertebra of the Patient TCGA-QQ-ASV2 using the 3DSlicer software.

The Field II simulation software [66, 67] was employed to simulate US images based on the CT scans. The simulated transducer assumes that the data were acquired with the patients in the prone position and the probe is perpendicular to the patients back. The transducer consists of 192 elements with 64 active elements at a time with the frequency of 3.6 MHz and propagation speed of 1540 m/s. In this simulation, Field II simulated 50 raw radio-frequency (RF) lines of data from 100,000 scatterers. Each scatterer point is randomly located in a continuous space from the corresponding interpolated CT image where a Gaussian noise was added with a mean of zero and unit variance as its parameters.

After generating simulated RF signals, 2D B-mode US images were created from the RF data by applying Hilbert transform in a slice-by-slice manner from the CT image. Then, all 2D US images were concatenated to reconstruct a 3D volume. Further, the constructed volumetric image was resampled to the resolution of the CT volumetric image. As the result, the US and CT images are well-aligned.

Since the simulator does not simulate shadowing of US below the bone surface, the back scatterers located below the bone surfaces will generate unrealistic echoes. Hence, the CT volumetric image was used as a template to correct the US image. The preprocessing method described in [49] was used to extract the bone surfaces of the CT image. The

transducer radiates the sound waves through the CT images and when they reach tissues with intensities T, it identifies the tissue as the bone surface. Consequently, the rest of the image in the waves direction would appear as a dark shadow. Heuristically, we found that $T = 270$ is the best value. Finally, the processed CT volumetric image was multiplied voxel-wise to the US volumetric image as a mask. Fig. 11 shows a slice of the simulated US images in the first row and in the second row, it displays the slice of the simulated US image overlaid on their corresponding CT image. The texture of the simulated US images is similar to real US images because they show the bone surfaces as back-scattered from the ultrasound wave. It is important to note that, there are shadows below the bone surfaces where the ultrasound wave could not penetrate the tissues. Inherently co-registered, the aligned CT and US images make a gold standard ground-truth to validate image registration algorithms.

4.2.2 Dog Vertebrae Phantom

The phantom gel was created using a mixture of water, Knox unflavored gelatin, sugar-free Metamucil psyllium fiber supplement [68], and a Rubbermaid Premium Dry Food Storage Canister to store the mixture. The canine spine model was formed using vinyl tubing, a wooden skewer,rubber O-rings, and 10 vertebrae, namely the section of the canine cervical vertebrae (C6-C7) and a section of the thoracic vertebrae (T1-T8).

The gel was prepared by bringing 3250 mL of water to a gentle simmer; however, the desired amount of gel was 2000 mL. There was a surplus of water to account for evaporation during the process. The gelatin was mixed with the water until it was completely dissolved. The ratio of water to gelatin was 28g of gelatin for every 250 mL of water [68]. Thus, a total of 224 g of gelatin was used for the desired amount of water. The Metamucil was subsequently added to the mixture in very small quantities to ensure that no lumps or bubbles formed. In total, an amount of 8 tablespoons of Metamucil were added to the mixture [68]. The mixture was then poured into the container and rested in the container until it had attained room temperature. The mixture was then placed in the refrigerator overnight to allow it to congeal [68].

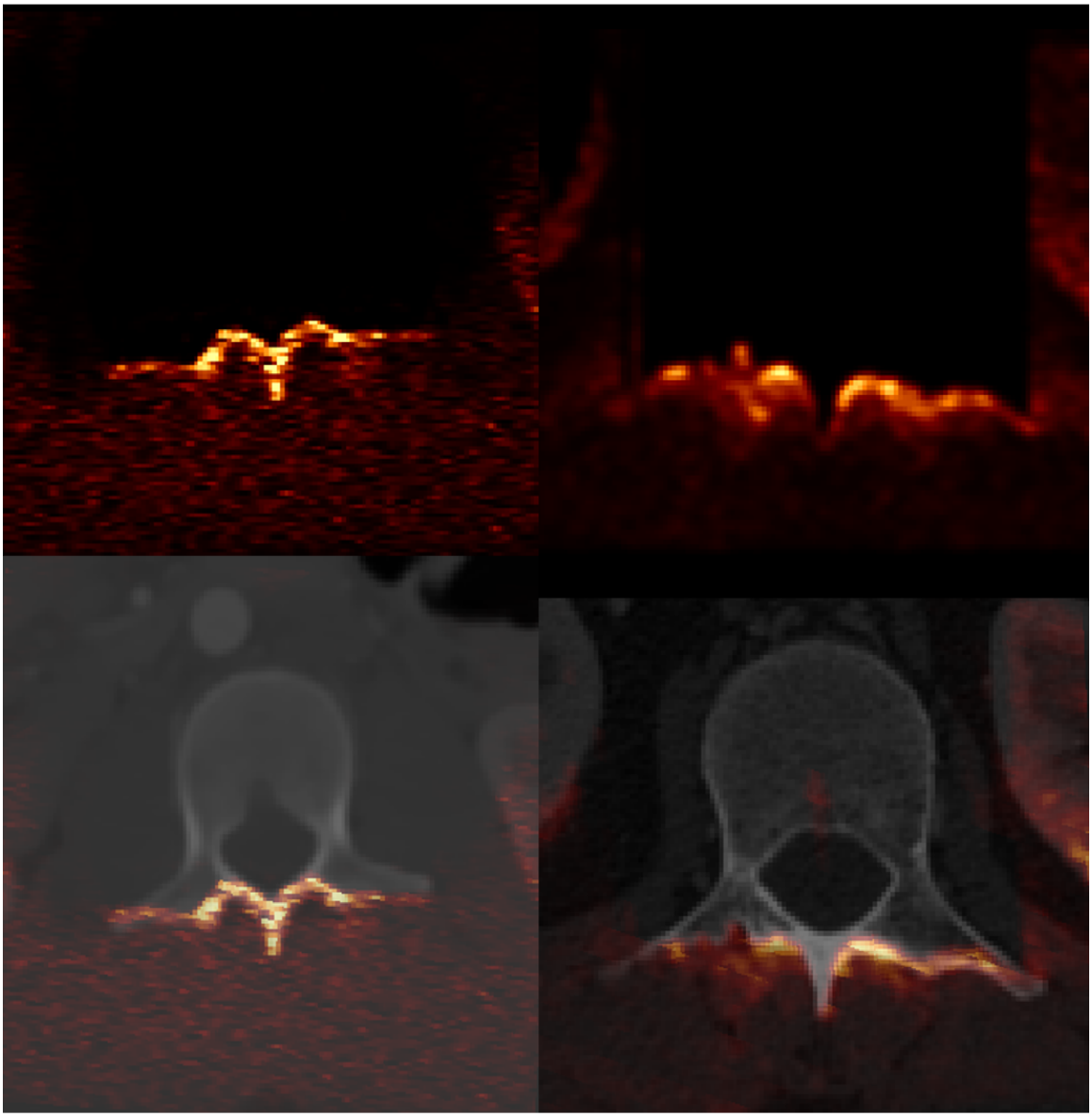

Figure 11: Axial view of a slice of simulated US images for Patient 1 (column 1) and Patient 2 (column 2) in the first row and overlaying of US images on their corresponding CT images in the second row. Note that the ultrasound probe is located in the bottom of the image.

Figure 12: Canine vertebrae, with the vinyl tubing inserted through the cavities and the rubber O-rings between each vertebrae, prior to complete immersion into the gel.

The vinyl tubing was cut to the length of the container and was inserted through the cavities in the middle of each vertebra. In between each vertebra, two rubber O-rings were placed to mimic the discs of the spine. A wooden stickcut the same length as the vinyl tubewas also inserted along the cavity of the vinyl tube to ensure that the spine model remained straight. Fig. 12 shows the canine vertebrae before having it immersed into the gel.

The solidified gel was placed in a bain-marie to heat the mixture so that it could liquefy without burning. Once the mixture became liquid, it was poured into a second container so that the spine model could be placed into the first. Once the spine model was fixed into placein the first containerthe mixture was slowly poured into the container so that no bubbles formed. The container with both the gel mixture and the spine model were placed in the refrigerator to solidify and was then used for experimentation and data acquisition.

The phantom CT scan was acquired at Concordia Universitys PERFORM centre in Montreal (Canada) using the CT scanner GE Discovery PET/CT 690 (Waukesha, WI) with the 7.4 90000133 L-Spine Survey Helical protocol. The CT image has $0.351 \times 0.351 mm^2$ in-slice resolution and $0.625 mm$ of slice thickness. The CT scan was executed so that the canine remained in the prone position with the orientation of the head facing the machine.

Following the CT scan, we acquired the spatially tracked US image of the phantom immediately to minimize any deformation of the phantom. The US image was acquired with an Alpinion E-CUBE 12R ultrasound machine (Bothell, WA) at the PERFORM centre. The SC1-4H curvilinear 2D phase array transducer was set to a frequency of 4.0 MHz and a depth of 10.0 cm. The US images were tracked with Northern Digital Inc. (NDI, Waterloo, ON) Polaris camera and NDI passive reflective markers. The US probe was calibrated before the acquiring the data. The ultrasound images have been recorded with the Ephiphan Systmes Inc. DVI2USB3.0 using the PLUS Toolkit [69], OpenIGTLink and the 3DSlicer accordingly as the acquisition software.

We provided 15 homologous tag-based landmarks in the US and CT images using the software register from MINC Toolkit (https://bic-mni.github.io). By employing the provided landmarks, we performed fiducial based registration with linear transformation using the 3DSlicer (https://www.slicer.org) and then resampled the US volumetric image to the CT volumetric image. As the result of the registration, the US and CT images are aligned with a silver standard ground truth. In the first row of Fig. 13, the C7 vertebra of the phantom is shown in the axial view and in the second and the third rows, the C7, C8, T1, and T2 vertebrae are displayed in sagittal and coronal views respectively. Columns one, two, and three display the CT, US, and overlaid the CT-US images respectively.

4.2.3 Lamb Vertebrae

Due to degenerative disc disease, 19% of working adults experience chronic low back pain (LBP) [70]. Each year there are many spinal fusion surgeries related to LBP which are performed on the lumbar region of the vertebrae. Lamb vertebrae are most similar to human vertebrae in lumbar and thoracic regions [71]. Herein, we acquired our data utilizing the L1-L5 vertebrae for a lamb.

To simulate the spine surgery, we created a surgical cavity on the posterior side of the vertebrae. We performed a dorsal midline incision and we removed the soft tissue over that area (Fig. 14a). A means for ultrasound imaging was created by absorbing the lumbar vertebrae into the same gel described earlier for the canine phantom (Fig. 14b).

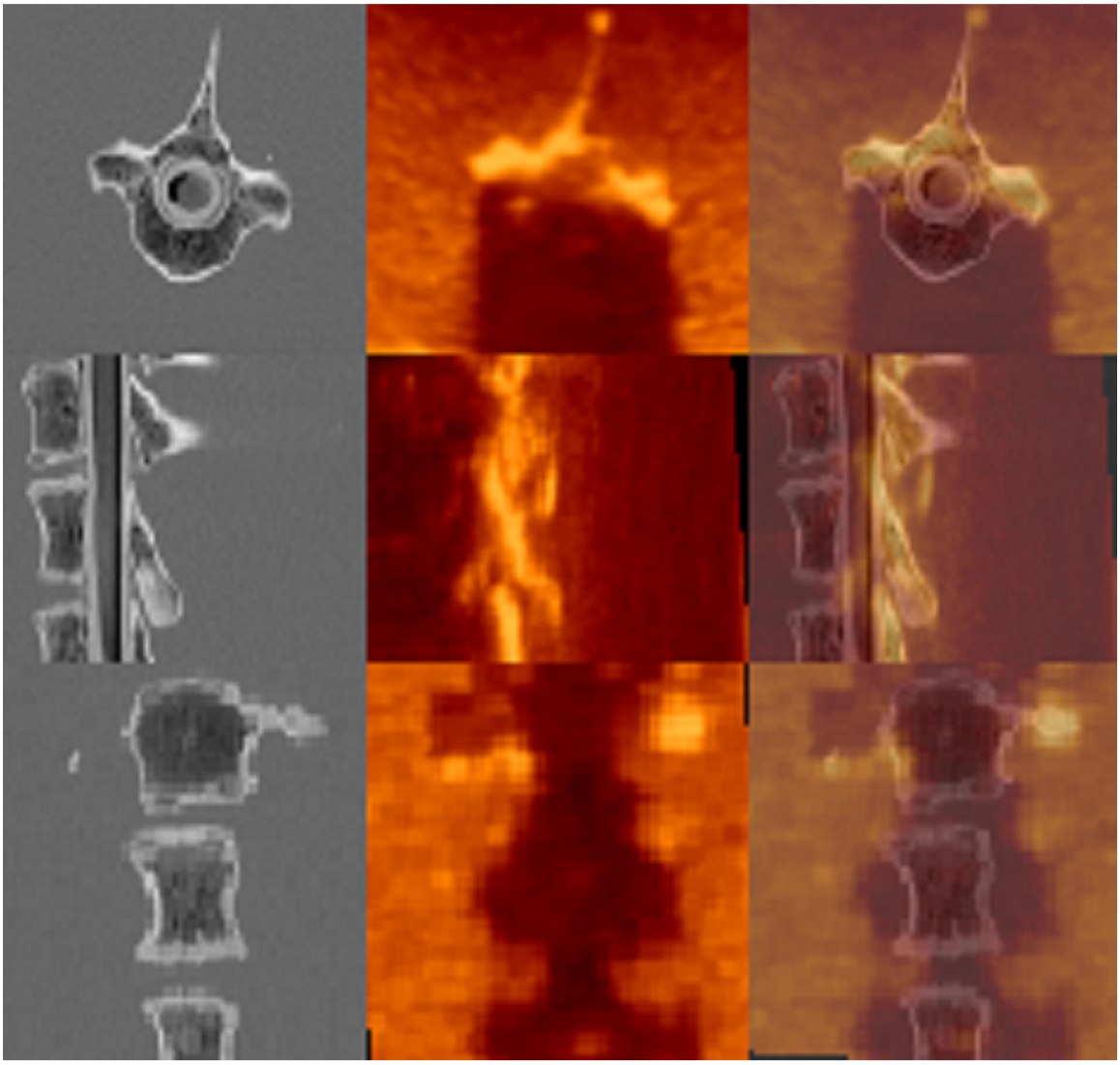

Figure 13: CT, US, and overlaid CT-US of the phantom from the left column respectively. The first, second, and third rows are axial, sagittal, and coronal views respectively.

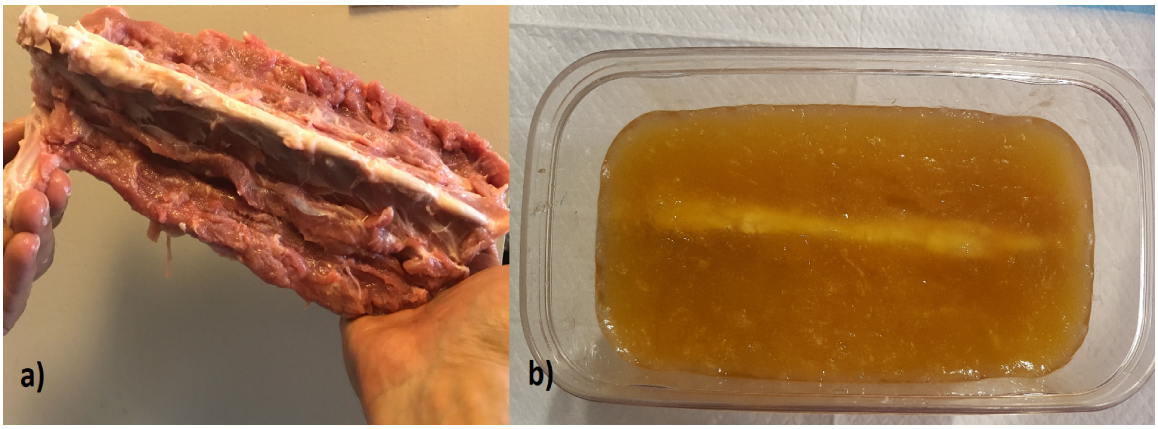

Figure 14: a) Lamb lumbar vertebrae before complete immersion into the gel and after removing the tissues over the dorsal midline. b) The lambs lumbar vertebrae after having been placed into the gel as a means to conduct the ultrasound imaging.

The procedure for both the CT and US data acquisition of the lamb lumbar remained the same as in the case of the canine phantom (Fig. 15).

The ultrasound volumetric image encompasses lumbar vertebrae from L2-L5 of the lamb. The 15 homologous anatomical landmarks were selected carefully using register from MINC Toolkit by N. Masoumi. Each vertebrae specific structures surfaces such as inferior facet, superior facet, spinous process, transverse process were the criteria for selecting the landmarks. Then, the fiducial-based registration was performed utilizing the landmarks to provide a silver standard ground truth for image registration techniques. Fig. 16 demonstrates the CT, US, and overlaid CT-US images of lumbar vertebrae from L2-L5 of the lamb in column one, two, and three respectively. The rows display the axial, sagittal, and coronal views respectively. The axial view displays one slice of the L4 lumbar vertebra.

4.3 Conclusion

Three datasets were outlined in this chapter. The simulation dataset can be too simplistic but offeres a gold standard registration between US and CT. The experimental datasets are very realistic but only offer a silver standard registration ground truth. Together, the simulation and experimental datasets can provide a complete validation set for validating

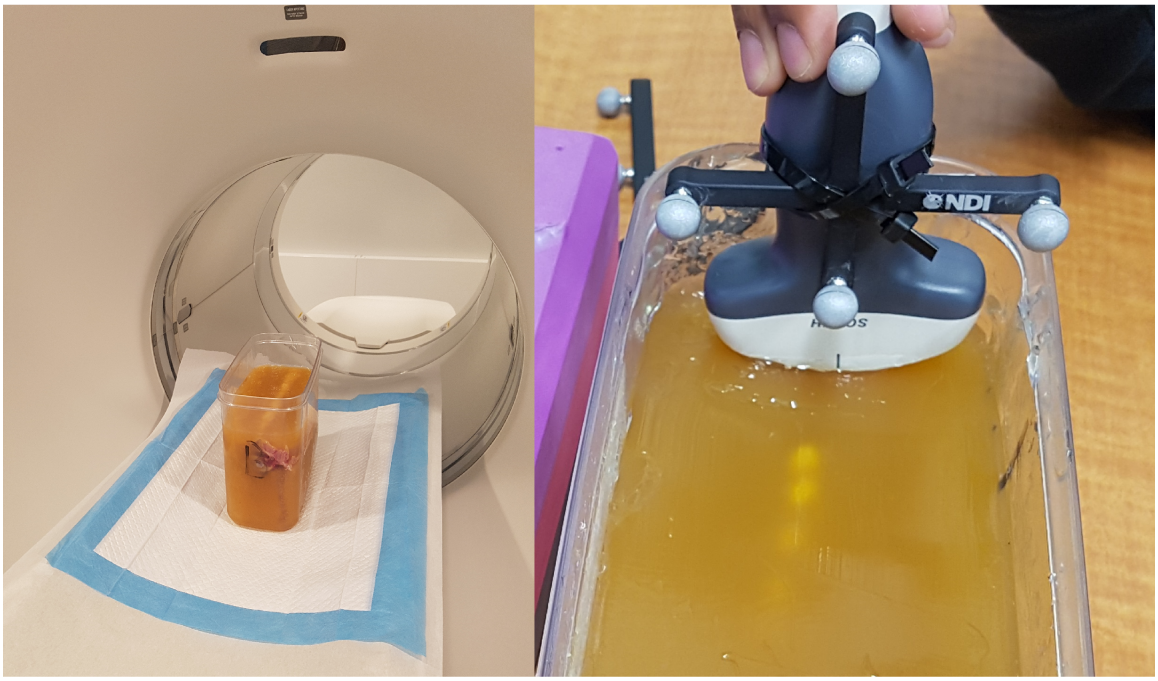

Figure 15: Imaging the lamb vertebrae phantom. Acquiring CT scan (left) and tracked ultrasound (right).

the accuracy of automatic image registration techniques.

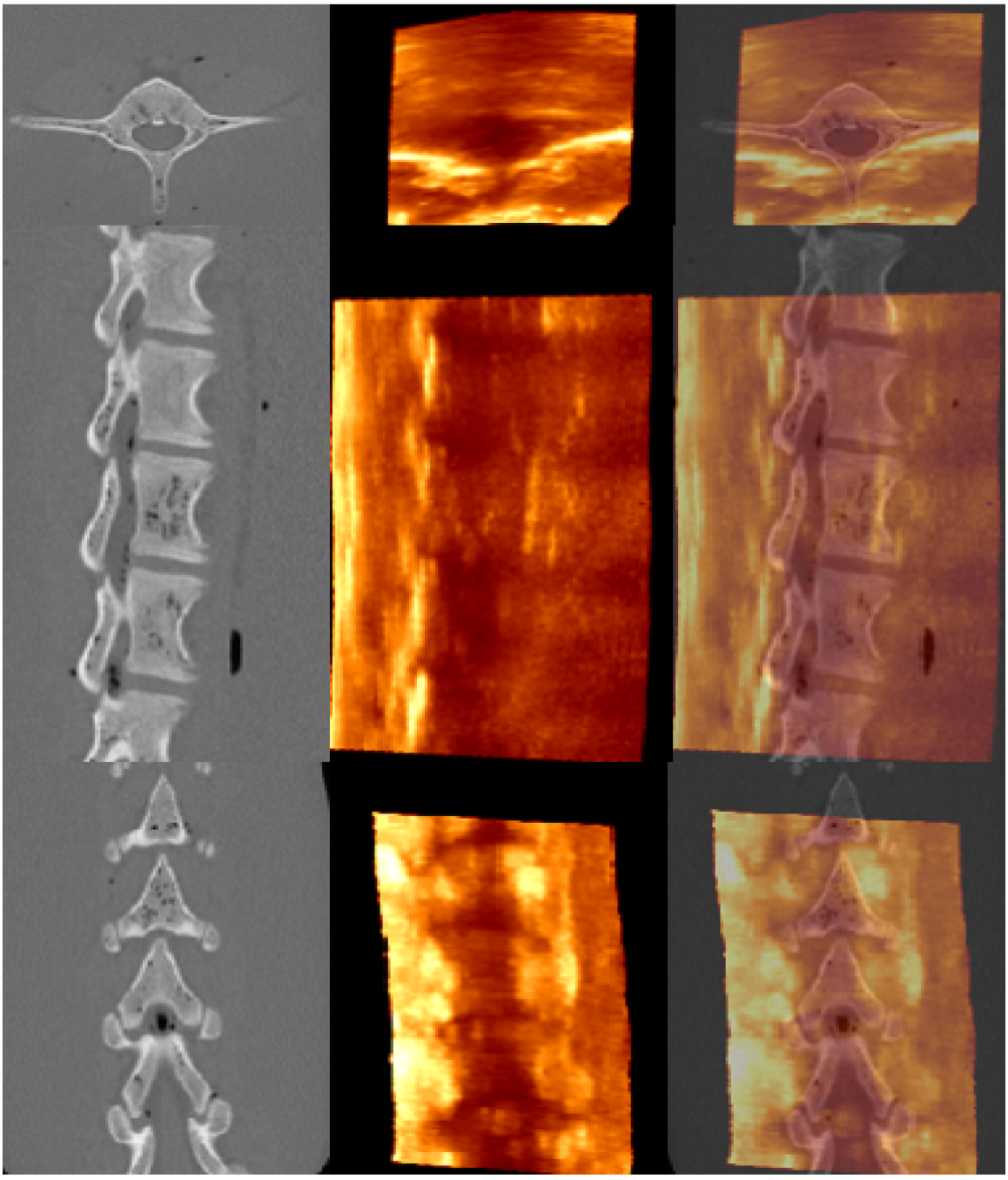

Figure 16: The axial, sagittal, and coronal views of the lamb lumbar vertebrae from the top row respectively. Columns from the left to the right show CT, US, and overlaid US on the CT image respectively.

Chapter 5

Conclusion, Discussions, and Future Work

5.1 Conclusion

In this thesis, two automatic inter-modality affine registration methods based on correlation ratio has been proposed. In Chapter 2, MARCEL was elaborated retrospectively for MRI-US registration in the context of brain shift correction during low-grade brain gliomas resection. From both quantitative and qualitative assessments, MARCEL has shown to successfully realign the intra-operative US with the pre-operative MRI scans.

MARCEL has been preliminary demonstrated using five brain cancer patients. RaPTOR was used as a similarity metric and mini-batch stochastic gradient descent as on optimizer. The refined version of MARCEL, ARENA, was validated on all the patients of the RESECT database. In ARENA the amended RaPTOR and the CMA-ES as the simirlarity metric and the optimizer was used respectively. ARENA was presented to align US and MRI volumetric images and was validated qualitatively and quantitatively. The qualitative results show that the registered images have improvements in alignment of salient image features. ARENA was compared with RaPTOR which is a deformable state-of-the-art image registration method. ARENA had overall advantage over RaPTOR especially in patients with higher initial mTRE wherein RaPTOR provided minimal improvements

in mTRE. ARENA has consistently improved the mTRE in all patients, and is therefore a potentially promising registration method for use during IGNS.

In Chapter 4, datasets of corresponding CT and US images were acquired and presented. The publicly available datasets are 3D ultrasound images of vertebrae which are hard to acquire, and as such, are rare. Simulated ultrasound images are more ideal images of vertebrae. They give gold standard ground-truth for validating image registration techniques. The canines thoracic vertebrae phantom and the lamb lumber vertebrae are more realistic data and challenging for multi-modal image registration algorithms. Provided landmark based landmarks give silver standard ground-truth for validation of image registration techniques.

5.2 Discussions

In optimization problems, the regularization term is defined as an additional information to prevent overfitting. Overfitting in the medical image registration context can be interpreted as existence of folds and/or ruptures in the tissues caused by the transformation. By using deformable transformations, exploiting a proper regularization term can result in a physically realistic image registration. Fundamental affine transformation properties such as collinearity, parallelism, and convexity can exempt affine transformation from generating the overfitting problem. In order to investigate this claim, we added regularization term to the optimization equation. As of expectation, the regularization term has not improved the results for either MARCEL or ARENA.

Image registration in medical applications is the process of aligning images where the alignment is validated by the clinicians, surgeons, and experts. Homologous landmark selection provides researchers a quantitative mean to validate the applied image registration methods. However, evaluation and validation of image registration methods with mTRE disregard pertinent features in the corresponding application. For instance, in the surgical oncology, generally the deformation of tissues around the tumor area is larger than the other regions after resection of the tumor. Therefore, the landmarks that are closer to the tumor

region require a larger transformation in order to achieve the image alignments criteria. Affine transformation may not be an appropriate transformation to attain the criteria. In validation of the ARENA with the RESECT database, the brain-shift can be sufficiently compensated with the affine transformation because the utilized intra-operative US images are acquired after opening of the dura and before resection of the tumor. In conclusion, before employing a transformation for a medical image registration method, we should select a proper transformation model for the application in hand.

5.3 Future Work

For the employment of ARENA in Chapter 3, CMA-ES implementation in MATLAB is not optimized and it is relatively slow with conventional CPUs. More specifically, for each hierarchical level the optimization takes $2 - 5$ minutes. Nevertheless, it is fast enough in IGNS settings where neurosurgeons generally spend about 10-20 min between collection of US images and resection of the tumor. For the next step, ARENA will be implemented with GPU in order to further accelerate the registration process. Finally, the aim is to further test ARENA on more datasets in different applications.

A rigid registration technique based on ARENA was implemented already and tested on the distributed CT-US datasets. In the near future, the rigid registration method will be validated with the distributed datasets decribed in Chapter 4. The goal is to reduce the registration execution time, because in real surgical procedures, the CT-US registration must be fast sufficiently to satisfy surgical requirements. So, the rigid registration algorithm will be implemented more efficiently in MATLAB to decrease the computational time.

For acquiring the data described in Chapter 4, we installed an IGS system at PERFORM Centre (Montreal, Canada). The image registration method has not been integrated to the IGS system yet. We plan to add the rigid image registration method to the processing unit of the IGS system, so that the image registration will be possible right after acquiring the data. The integration of the image registration to the IGS system is important especially when we are aquiring data from human patients. Consequently, we will emulate the IGS

systems in the operation rooms.

Bibliography

[1] B. Zitova and J. Flusser, "Image registration methods: a survey," *Image and vision computing*, vol. 21, no. 11, pp. 977–1000, 2003.

[2] H. Ghassemian, "A review of remote sensing image fusion methods," *Information Fusion*, vol. 32, pp. 75–89, 2016.

[3] M. Ghahremani and H. Ghassemian, "Remote sensing image fusion using ripplet transform and compressed sensing," *IEEE Geoscience and Remote Sensing Letters*, vol. 12, no. 3, pp. 502–506, 2015.

[4] L. Alparone, B. Aiazzi, S. Baronti, and A. Garzelli, *Remote sensing image fusion*. Crc Press, 2015.

[5] A. P. James and B. V. Dasarathy, "Medical image fusion: A survey of the state of the art," *Information Fusion*, vol. 19, pp. 4–19, 2014.

[6] L. Wang, B. Li, and L.-F. Tian, "Multi-modal medical image fusion using the inter-scale and intra-scale dependencies between image shift-invariant shearlet coefficients," *Information Fusion*, vol. 19, pp. 20–28, 2014.

[7] G. Bhatnagar, Q. J. Wu, and Z. Liu, "A new contrast based multimodal medical image fusion framework," *Neurocomputing*, vol. 157, pp. 143–152, 2015.

[8] R. Shams, Y. Xiao, F. Hébert, M. Abramowitz, R. Brooks, and H. Rivaz, "Assessment of rigid registration quality measures in ultrasound-guided radiotherapy," *IEEE transactions on medical imaging*, vol. 37, no. 2, pp. 428–437, 2018.

[9] A. J. Golby, *Image-guided neurosurgery*. Academic Press, 2015.

[10] N. Farhat, T. Kapur, and R. Kikinis, "Role of computers and image processing in image-guided brain tumor surgery," in *Image-Guided Neurosurgery*, pp. 143–161, Elsevier, 2015.

[11] P. C. Warnke and A. Ralston, "Image-guided brain biopsy," in *Image-Guided Neurosurgery*, pp. 193–211, Elsevier, 2015.

[12] P. M. Patel and V. M. Shah, "Image registration techniques: a comprehensive survey," *International Journal of Innovative Research and Development*, 2014.

[13] S. Saxena and R. K. Singh, "A survey of recent and classical image registration methods," *International journal of signal processing, image processing and pattern recognition*, vol. 7, no. 4, pp. 167–176, 2014.

[14] F. P. Oliveira and J. M. R. Tavares, "Medical image registration: a review," *Computer methods in biomechanics and biomedical engineering*, vol. 17, no. 2, pp. 73–93, 2014.

[15] S. W. Teng, M. T. Hossain, and G. Lu, "Multimodal image registration technique based on improved local feature descriptors," *Journal of Electronic Imaging*, vol. 24, no. 1, p. 013013, 2015.

[16] M. P. Heinrich, M. Jenkinson, M. Bhushan, T. Matin, F. V. Gleeson, M. Brady, and J. A. Schnabel, "Mind: Modality independent neighbourhood descriptor for multimodal deformable registration," *Medical image analysis*, vol. 16, no. 7, pp. 1423–1435, 2012.

[17] T. Hopp, M. Dietzel, P. A. Baltzer, P. Kreisel, W. A. Kaiser, H. Gemmeke, and N. V. Ruiter, "Automatic multimodal 2d/3d breast image registration using biomechanical fem models and intensity-based optimization," *Medical image analysis*, vol. 17, no. 2, pp. 209–218, 2013.

[18] Y. Hu, M. Modat, E. Gibson, W. Li, N. Ghavami, E. Bonmati, G. Wang, S. Bandula, C. M. Moore, M. Emberton, *et al.*, "Weakly-supervised convolutional neural networks for multimodal image registration," *Medical image analysis*, 2018.

[19] H. Zhou and H. Rivaz, "Registration of pre-and postresection ultrasound volumes with noncorresponding regions in neurosurgery," *IEEE journal of biomedical and health informatics*, vol. 20, no. 5, pp. 1240–1249, 2016.

[20] D. Loeckx, P. Slagmolen, F. Maes, D. Vandermeulen, and P. Suetens, "Nonrigid image registration using conditional mutual information," *IEEE transactions on medical imaging*, vol. 29, no. 1, pp. 19–29, 2010.

[21] M. Deshmukh and U. Bhosle, "A survey of image registration," *International Journal of Image Processing (IJIP)*, vol. 5, no. 3, p. 245, 2011.

[22] H. Rivaz and D. L. Collins, "Deformable registration of preoperative mr, pre-resection ultrasound, and post-resection ultrasound images of neurosurgery," *International journal of computer assisted radiology and surgery*, vol. 10, no. 7, pp. 1017–1028, 2015.

[23] A. Roche, G. Malandain, N. Ayache, and X. Pennec, *Multimodal image registration by maximization of the correlation ratio*. PhD thesis, INRIA, 1998.

[24] A. Roche, X. Pennec, M. Rudolph, D. Auer, G. Malandain, S. Ourselin, L. M. Auer, and N. Ayache, "Generalized correlation ratio for rigid registration of 3d ultrasound with mr images," in *International Conference on Medical Image Computing and Computer-Assisted Intervention*, pp. 567–577, Springer, 2000.

[25] M. Holden, "A review of geometric transformations for nonrigid body registration," *IEEE transactions on medical imaging*, vol. 27, no. 1, p. 111, 2008.

[26] S. Klein, M. Staring, and J. P. Pluim, "Evaluation of optimization methods for nonrigid medical image registration using mutual information and b-splines," *IEEE transactions on image processing*, vol. 16, no. 12, pp. 2879–2890, 2007.

[27] Y. Xiao, M. Fortin, G. Unsgård, H. Rivaz, and I. Reinertsen, "Retrospective evaluation of cerebral tumors (resect): a clinical database of pre-operative mri and intra-operative ultrasound in low-grade glioma surgeries," *Medical Physics*, 2017.

[28] N. Masoumi, Y. Xiao, and H. Rivaz, "Marcel (inter-modality affine registration with correlation ratio): An application for brain shift correction in ultrasound-guided brain tumor resection," in *International MICCAI Brainlesion Workshop*, pp. 55–63, Springer, 2018.

[29] E. C. Holland, "Progenitor cells and glioma formation," *Current opinion in neurology*, vol. 14, no. 6, pp. 683–688, 2001.

[30] T. A. Dolecek, J. M. Propp, N. E. Stroup, and C. Kruchko, "Cbtrus statistical report: primary brain and central nervous system tumors diagnosed in the united states in 2005–2009," *Neuro-oncology*, vol. 14, no. suppl 5, pp. v1–v49, 2012.

[31] I. J. Gerard, M. Kersten-Oertel, K. Petrecca, D. Sirhan, J. A. Hall, and D. L. Collins, "Brain shift in neuronavigation of brain tumors: A review," *Medical image analysis*, vol. 35, pp. 403–420, 2017.

[32] D. De Nigris, D. L. Collins, and T. Arbel, "Multi-modal image registration based on gradient orientations of minimal uncertainty," *IEEE transactions on medical imaging*, vol. 31, no. 12, pp. 2343–2354, 2012.

[33] H. Rivaz, S. J.-S. Chen, and D. L. Collins, "Automatic deformable mr-ultrasound registration for image-guided neurosurgery," *IEEE transactions on medical imaging*, vol. 34, no. 2, pp. 366–380, 2015.

[34] H. Rivaz and D. L. Collins, "Near real-time robust non-rigid registration of volumetric ultrasound images for neurosurgery," *Ultrasound in medicine & biology*, vol. 41, no. 2, pp. 574–587, 2015.

[35] P. Daga, G. Winston, M. Modat, M. White, L. Mancini, M. J. Cardoso, M. Symms, J. Stretton, A. W. McEvoy, J. Thornton, *et al.*, "Accurate localization of optic radiation

during neurosurgery in an interventional mri suite," *IEEE transactions on medical imaging*, vol. 31, no. 4, pp. 882–891, 2012.

[36] S. Damas, O. Cordón, and J. Santamaría, "Medical image registration using evolutionary computation: An experimental survey," *IEEE Computational Intelligence Magazine*, vol. 6, no. 4, pp. 26–42, 2011.

[37] J. Ma, H. Zhou, J. Zhao, Y. Gao, J. Jiang, and J. Tian, "Robust feature matching for remote sensing image registration via locally linear transforming," *IEEE Transactions on Geoscience and Remote Sensing*, vol. 53, no. 12, pp. 6469–6481, 2015.

[38] S. Li, X. Kang, L. Fang, J. Hu, and H. Yin, "Pixel-level image fusion: A survey of the state of the art," *Information Fusion*, vol. 33, pp. 100–112, 2017.

[39] Y. Yang, Y. Que, S. Huang, and P. Lin, "Multimodal sensor medical image fusion based on type-2 fuzzy logic in nsct domain," *IEEE Sensors Journal*, vol. 16, no. 10, pp. 3735–3745, 2016.

[40] L. Besharati Tabrizi and M. Mahvash, "Augmented reality–guided neurosurgery: accuracy and intraoperative application of an image projection technique," *Journal of neurosurgery*, vol. 123, no. 1, pp. 206–211, 2015.

[41] C. R. Maurer and J. M. Fitzpatrick, "A review of medical image registration," *Interactive image-guided neurosurgery*, vol. 1, pp. 17–44, 1993.

[42] S. Nag, "Image registration techniques: A survey," *arXiv preprint arXiv:1712.07540*, 2017.

[43] M. A. Viergever, J. A. Maintz, S. Klein, K. Murphy, M. Staring, and J. P. Pluim, "A survey of medical image registration–under review," *Medical image analysis*, vol. 33, pp. 140–144, 2016.

[44] M. Gong, S. Zhao, L. Jiao, D. Tian, and S. Wang, "A novel coarse-to-fine scheme for automatic image registration based on sift and mutual information," *IEEE Transactions on Geoscience and Remote Sensing*, vol. 52, no. 7, pp. 4328–4338, 2014.

[45] H. J. Johnson and G. E. Christensen, "Consistent landmark and intensity-based image registration," *IEEE transactions on medical imaging*, vol. 21, no. 5, pp. 450–461, 2002.

[46] G. Chandrashekar and F. Sahin, "A survey on feature selection methods," *Computers & Electrical Engineering*, vol. 40, no. 1, pp. 16–28, 2014.

[47] D. Rueckert and P. Aljabar, "Nonrigid registration of medical images: Theory, methods, and applications [applications corner]," *IEEE Signal Processing Magazine*, vol. 27, no. 4, pp. 113–119, 2010.

[48] A. Sotiras, C. Davatzikos, and N. Paragios, "Deformable medical image registration: A survey," *IEEE transactions on medical imaging*, vol. 32, no. 7, pp. 1153–1190, 2013.

[49] C. X. Yan, B. Goulet, J. Pelletier, S. J.-S. Chen, D. Tampieri, and D. L. Collins, "Towards accurate, robust and practical ultrasound-ct registration of vertebrae for image-guided spine surgery," *International journal of computer assisted radiology and surgery*, vol. 6, no. 4, pp. 523–537, 2011.

[50] S. Gill, P. Abolmaesumi, G. Fichtinger, J. Boisvert, D. Pichora, D. Borshneck, and P. Mousavi, "Biomechanically constrained groupwise ultrasound to ct registration of the lumbar spine," *Medical image analysis*, vol. 16, no. 3, pp. 662–674, 2012.

[51] I. Hacihaliloglu, A. Rasoulian, R. N. Rohling, and P. Abolmaesumi, "Local phase tensor features for 3-d ultrasound to statistical shape+ pose spine model registration," *IEEE transactions on Medical Imaging*, vol. 33, no. 11, pp. 2167–2179, 2014.

[52] G. Balakrishnan, A. Zhao, M. R. Sabuncu, J. Guttag, and A. V. Dalca, "An unsupervised learning model for deformable medical image registration," in *Proceedings of the IEEE Conference on Computer Vision and Pattern Recognition*, pp. 9252–9260, 2018.

[53] O. Weistrand and S. Svensson, "The anaconda algorithm for deformable image registration in radiotherapy," *Medical physics*, vol. 42, no. 1, pp. 40–53, 2015.

[54] B. Zhao, G. E. Christensen, J. Hyun Song, Y. Pan, S. E. Gerard, J. M. Reinhardt, K. Du, T. Patton, J. M. Bayouth, and G. D. Hugo, "Tissue-volume preserving deformable image registration for 4dct pulmonary images," in *Proceedings of the IEEE Conference on Computer Vision and Pattern Recognition Workshops*, pp. 41–49, 2016.

[55] F. Maes, D. Loeckx, D. Vandermeulen, and P. Suetens, "Image registration using mutual information," in *Handbook of Biomedical Imaging*, pp. 295–308, Springer, 2015.

[56] N. Hansen and A. Ostermeier, "Adapting arbitrary normal mutation distributions in evolution strategies: The covariance matrix adaptation," in *Evolutionary Computation, 1996., Proceedings of IEEE International Conference on*, pp. 312–317, IEEE, 1996.

[57] I. Machado, M. Toews, J. Luo, P. Unadkat, W. Essayed, E. George, P. Teodoro, H. Carvalho, J. Martins, P. Golland, and S. Pieper, "Non-rigid registration of 3d ultrasound for neurosurgery using automatic feature detection and matching," *International journal of computer assisted radiology and surgery*, pp. 1–14, 2018.

[58] E. Reinhard, W. Heidrich, P. Debevec, S. Pattanaik, G. Ward, and K. Myszkowski, *High dynamic range imaging: acquisition, display, and image-based lighting*. Morgan Kaufmann, 2010.

[59] B. Fischer and J. Modersitzki, "Ill-posed medicinean introduction to image registration," *Inverse Problems*, vol. 24, no. 3, p. 034008, 2008.

[60] N. Hansen and A. Ostermeier, "Completely derandomized self-adaptation in evolution strategies," *Evolutionary computation*, vol. 9, no. 2, pp. 159–195, 2001.

[61] J. M. Fitzpatrick, "Fiducial registration error and target registration error are uncorrelated," in *Medical Imaging 2009: Visualization, Image-Guided Procedures, and Modeling*, vol. 7261, p. 726102, International Society for Optics and Photonics, 2009.

[62] J. D. Gibbons and S. Chakraborti, "Nonparametric statistical inference," in *International encyclopedia of statistical science*, pp. 977–979, Springer, 2011.

[63] Y. Xiao, L. Eikenes, I. Reinertsen, and H. Rivaz, "Nonlinear deformation of tractography in ultrasound-guided low-grade gliomas resection," *International journal of computer assisted radiology and surgery*, vol. 13, no. 3, pp. 469–469, 2018.

[64] K. Clark, B. Vendt, K. Smith, J. Freymann, J. Kirby, P. Koppel, S. Moore, S. Phillips, D. Maffitt, M. Pringle, *et al.*, "The cancer imaging archive (tcia): maintaining and operating a public information repository," *Journal of digital imaging*, vol. 26, no. 6, pp. 1045–1057, 2013.

[65] C. Roche, E. Bonaccio, and J. Filippini, "Radiology data from the cancer genome atlas sarcoma [tcga-sarc] collection," *The Cancer Imaging Archive*, 2016.

[66] J. A. Jensen, "Field: A program for simulating ultrasound systems," in *10TH NORDICBALTIC CONFERENCE ON BIOMEDICAL IMAGING, VOL. 4, SUPPLEMENT 1, PART 1: 351–353*, Citeseer, 1996.

[67] J. A. Jensen and N. B. Svendsen, "Calculation of pressure fields from arbitrarily shaped, apodized, and excited ultrasound transducers," *IEEE transactions on ultrasonics, ferroelectrics, and frequency control*, vol. 39, no. 2, pp. 262–267, 1992.

[68] J. L. Kendall and J. P. Faragher, "Ultrasound-guided central venous access: a homemade phantom for simulation," *Canadian Journal of Emergency Medicine*, vol. 9, no. 5, pp. 371–373, 2007.

[69] A. Lasso, T. Heffter, A. Rankin, C. Pinter, T. Ungi, and G. Fichtinger, "Plus: open-source toolkit for ultrasound-guided intervention systems," *IEEE Transactions on Biomedical Engineering*, vol. 61, no. 10, pp. 2527–2537, 2014.

[70] F. M. Phillips, P. J. Slosar, J. A. Youssef, G. Andersson, and F. Papatheofanis, "Lumbar spine fusion for chronic low back pain due to degenerative disc disease: a systematic review," *Spine*, vol. 38, no. 7, pp. E409–E422, 2013.

[71] H.-J. Wilke, A. Kettler, K. H. Wenger, and L. E. Claes, "Anatomy of the sheep spine and its comparison to the human spine," *The Anatomical Record: An Official Publication of the American Association of Anatomists*, vol. 247, no. 4, pp. 542–555, 1997.